1-1-1998

The evolution of order in liquid crystals and polymer crystals.

Chester, Liu
University of Massachusetts Amherst

THE EVOLUTION OF ORDER IN LIQUID CRYSTALS AND POLYMER CRYSTALS

A Dissertation Presented

by

CHESTER LIU

Submitted to the Graduate School of the

University of Massachusetts Amherst in partial fulfillment

of the requirements for the degree of

DOCTOR OF PHILOSOPHY

May 1998

Department of Polymer Science and Engineering

THE EVOLUTION OF ORDER IN LIQUID CRYSTALS AND POLYMER CRYSTALS

A Dissertation Presented

by

CHESTER LIU

Approved as to style and content by:

M. Muthukumar, Chair

David A. Hoagland, Member

David A. Tirrell, Member

Richard Farris, Department Head
Polymer Science and Engineering

ACKNOWLEDGMENTS

I am most grateful to my advisor, Prof. M. Mathukumar, for his guidance and support over the years. He has rightfully won numerous awards over the years for his groundbreaking work in many subjects. Despite his reputation as an intellectual powerhouse and excellent lecturer, he is not only interested in his students producing results and papers – he has invested much personal time and energy in improving their communication skills, in stimulating discussions on just about any subject, and in the many fine dinners we had at his home. I thank him for being not just an advisor, but a friend.

I am also grateful to my committee members, Prof. D. Tirrell and Prof. D. Hoagland for their time, patience, and insightful questions and comments. Their graciousness will not be forgotten.

I sincerely appreciate the stimulating discussions, debates, and most of all, friendship from the members of my group who have made these years so much more enjoyable both in and outside of the lab. They are: Y. Akpalu, G. Carri, C. Y. Huang, L. Kielhorn, J. Kong, R. Mondescu, D. Petera, V. Prabhu, F. von Goeler, and P. Welch.

In addition, I wish to thank my friends of all ages and all continents (except Antarctica) who worship at the First Baptist Church of Amherst. Through their selfless love and service they exemplify the love of Jesus Christ and the fellowship of believers.

Finally, without my family I would not be here, and I thank them for standing by me regardless of the choices I have made in life and the successes and failures I have encountered. Thanks, mom, dad, and sis!

ABSTRACT

THE EVOLUTION OF ORDER IN LIQUID CRYSTALS AND POLYMER CRYSTALS

MAY 1998

CHESTER LIU, B.S., MASSACHUSETTS INSTITUTE OF TECHNOLOGY

M.S., MASSACHUSETTS INSTITUTE OF TECHNOLOGY

Ph.D., UNIVERSITY OF MASSACHUSETTS AMHERST

Directed by: Professor M. Muthukumar

This dissertation describes computer simulations and theoretical analyses of ordering processes in liquid crystals and polymers. One ordering process in liquid crystals occurs during the isotropic to nematic transition in which point and line defects form and annihilate. Monte Carlo simulations support the newly-derived scaling of the defect density, which was found to scale with time as -6/7 in both two and three dimensions, contrary to the mean-field result of -1. Frustration was determined to be a key factor in this difference.

Another ordering process in liquid crystals is the evolution of inversion walls and loops. Analogous to the model of a shrinking elastic loop in a viscous medium which has been theoretically investigated by deGennes and Brochard, our lattice Monte Carlo simulations of inversion walls and loops show the same scaling behavior with time and the same predicted dependence of shrinkage rate on the orientational diffusion coefficient.

Polymer crystallization constitutes the other major topic of this dissertation. The initial stages of crystallization are difficult to study experimentally but by using the united-atom Langevin dynamics method, single and multi-chain crystallization can be simulated. The simulations show that random fluctuations nucleate regions of higher order which in turn can induce further crystallization. Lamellar thicknesses obtained from simulations at various undercoolings showed the same scaling behavior as experimental data from literature. Besides homogeneous nucleation, secondary nucleation was also observed, with the newly-attached chains continuing to undergo conformational changes on the crystal surface. Finally, the phenomenon of lamellar thickening was investigated. Lamellar thickening was observed to occur cooperatively in a stepwise, quantized manner.

TABLE OF CONTENTS

LIST OF FIGURES

CHAPTER 1

INTRODUCTION

1.1 Organization

Due to the self-contained nature of the topics in this dissertation, the theory and literature review sections commonly found in the introductory chapter are to be found in later chapters together with related data and discussions. Instead, chapter 1 covers the underlying and unifying themes of this research and discusses the relevant concepts and ideas.

Chapter 2 addresses the annihilation kinetics of liquid crystal defects in two and three dimensions. Simulations are performed under various conditions and the results are compared to theoretical predictions and experimental results.

The work described in Chapter 3 is similar to chapter 2 in that it also employs the Monte Carlo method to simulate liquid crystals. However, the focus is on inversion walls. Instead of being an disorder-order transition of the type described in chapter 2, inversion wall formation and decay is an order-order transition. Again, comparison will be made with theory and experiment.

Chapter 4 describes how simulation is used to answer the question of how polymers crystallize. Attention will be given to single and multi-chain crystallization, primary and secondary nucleation, and lamellar thickening.

Finally, chapter 5 will provide a brief summary of the most important results and suggest possible future work.

1.2 Themes

The three main chapters of this thesis can be subdivided according to several common themes. An understanding of these themes will enable the reader to understand the thesis in a broader context.

1.2.1 Subject Matter

One logical subdivision is along the line of subject matter. The liquid crystal defect annihilation problem and inversion wall problem both deal with nematic liquid crystals whereas the polymer crystallization problem deals with polymers. However, the existence of polymer liquid crystals has been known since the 1950's and has been studied by many groups. [1–4] Polymer liquid crystals bridge the gap between small-molecule liquid crystals and polymers in many ways. Main-chain polymer liquid crystals contain mesogenic moieties along the backbone while side-chain polymer liquid crystals contain such moieties on side chains. Polymer liquid crystals exhibit the same properties as small-molecule liquid crystals, such as birefringence, anisotropy, and electric and magnetic susceptibility. They also share the same abundance of point and line defects. Compared with small-molecule liquid crystals, polymer liquid crystals have higher viscosities and much higher splay moduli due to the constraints arising from chain connectivity. [5] The latter property has an useful side effect, allowing defect textures to be easily frozen and examined under the microscope.

1.2.2 Process

Another logical subdivision is by process. Both liquid crystal defect annihilation and polymer crystallization deal with the process of crystallization, the difference

being that in polymer crystallization we are more concerned with the crystal itself whereas in liquid crystal defect annihilation we are more concerned with the non-crystalline part, also known as defects. Commonly, the non-crystalline portion of a polymer lamella is called the amorphous region. The amorphous region contains many defects rather than single, isolated point defects. During any kind of crystallization, an alignment process is necessary to produce orientational order. The driving forces towards order seem different for defect annihilation versus polymer crystallization but in fact are similar. In both cases there is attraction between molecules, but beyond that, liquid crystals, being rigid rods, align due to simple geometric constraints and packing considerations, while for polymers which remain as amorphous globules, the alignment is due to both stereoregularity and steric constraints which dictate the torsional potential function, which below the crystallization temperature energetically favors the straight chain conformation. The consequence of all this argument is that local geometry is a very important element in any formation of ordered systems. For example, small changes in molecular geometry are responsible for the myriad forms of micelles, from spherical to tubular to vesicular.

Inversion wall formation and decay represents a different process, the order-order transition. [6–9] The intermediate state, where the inversion wall exists, can be viewed as a state of partial disorder, much like grain boundaries in a polycrystalline metal. Nematic liquid crystals exhibit this behavior because their orientation is described by a director, which unlike a vector, has no distinction between head and tail. Before the formation of inversion walls, the liquid crystals are in a monodomain, all in the same orientation. An electric or magnetic field is then applied in an orthogonal direction. Since liquid crystals with positive susceptibilities tend to align with the field, they must rotate, but due to the ambiguous nature of the

director orientation, both positive and negative directions of rotation are equal, or degenerate. Domains of positive and negative rotations develop, and where these domains impinge, inversion walls are formed. Inversion walls are thus named because across the wall, director orientation inverts by 180 degrees. Walls can be classified according to several types, the details of which are found in chapter 3. In any case, the existence of these walls represents an energy barrier which must be overcome by a decrease of the wall length. This is often manifested when one domain is surrounded by another, and the ring that separates them contracts. The distinguishing feature of inversion wall formation and decay is that the initial and final states are identical and that the walls are transient.

1.2.3 Simulation Method

Molecular motion is simulated by the time integration of a potential energy function or force field. Often, the goal is to explore the potential energy landscape in search of the global minimum or to assemble the probability distribution of various configurations. Possible choices of methodologies to simulate molecular motion ranges from the stochastic end of the spectrum, e.g. Monte Carlo method, [10] to the deterministic end of the spectrum, e.g. the Newtonian dynamics method. [11] In between these two ends are hybrid Monte Carlo methods and the Langevin and Brownian dynamics methods. Deterministic methods are exact spatially and temporally, but they pay the price by having to account for every molecule, which can slow the simulation dramatically and explore very little phase space. Typical molecular dynamics simulations can only simulate picoseconds to nanoseconds of realtime, not enough to simulate any but the smallest and fastest processes. Stochastic methods, on the other hand, trade off exactness for speed. Spatial and

temporal continuity may be lost, but equilibrium thermodynamic statistics can be generated with great ease and are useful for simulating processes which take place on the order of microseconds.

Intermediate methods borrow features from both extremes. For example, hybrid Monte Carlo methods alternate between periods when Monte Carlo is used and when molecular dynamics is used. The purpose is that Monte Carlo allows for large jumps in phase space while molecular dynamics can probe a local set of configurations intensively. This may result in a faster search for the global minimum. Langevin dynamics is basically Newtonian dynamics with a fluctuation-dissipation (noise) term included to simulate the effect of a solvent. The advantage is non-trivial because in simulations of solutions, solute molecules are often greatly outnumbered by solvent molecules.

The choice of simulation method is an important consideration both in generating the type of data needed for the study and in the efficiency of the methodology. Two methods, Monte Carlo and Langevin dynamics, were used during the course of this research. Both liquid crystal simulations were performed with Monte Carlo techniques while the polymer crystallization simulation was performed with Langevin dynamics. The details of Monte Carlo, or more specifically, the Metropolis algorithm, can be found in chapter 2. Here, we will review some of its distinguishing features. The Metropolis algorithm is basically a process by which random sampling of phase space is weighted by the probability based on the hamiltonian. Low-energy configurations are more favorable than high-energy configurations. The Metropolis algorithm is well-suited for equilibrium studies because it can sample a large phase space quickly. It is also well-suited for situations when the free energy function is readily available but its gradient, the force field, is not easily calculated. This is one reason it was chosen for the liquid crystal simulations because

the Frank free energy elegantly uses the bend, twist, and splay elastic constants to describe the interaction between nematic directors. For non-equilibrium studies such as the liquid crystal quench in this thesis, kinetic information is a bit more difficult to obtain due to the non-linear correspondence of simulation time to real time. The solution is to make the simulation time steps smaller which will make the simulation time nearly linear with real time.

A Metropolis simulation performed in the limit of small time steps actually straddles the divide between stochastic and deterministic methods. This is because as the step size decreases, the number of iterations per real time increases and according to the law of averages the result will converge with the result given by deterministic methods. Of course, the main reason for choosing the Metropolis algorithm is so that large time scales can be simulated, but nonetheless it is interesting to see that the integration methods are not so different after all.

Langevin dynamics as mentioned previously is similar to molecular dynamics with extra terms to account for the implicit effect of random collisions with solvent particles. [12] It includes terms from the fluctuation-dissipation theorem, which states that collisions with solvent molecules induce fluctuations as well as impart viscous drag. More details are found in chapter 4. This technique is ideally suited for simulating polymers in solution, and we have applied it to dilute solution polymer crystallization.

1.3 Goals

There are several goals we wish to accomplish in this research. One is to better understand the kinetic aspects of various processes, a question of exactly how one got from point A to point B rather than simply comparing point A with point

B. With liquid crystal defect annihilation for example, it is important and interesting to see whether defects usually take tortuous or linear paths on their way to mutual annihilation. Knowing this path would help answer the question as to why the actual rate of annihilation is slower than that predicted by mean-field theory. With polymer crystallization, one is curious as to whether chain folding begins at chain ends or in the middle, how a lamella undergoes thickening, or how free-floating molecules crystallize onto a surface. This study makes heavy use of graphic visualization.

The second goal is to be able to compare simulations with experimental results, not only because the comparisons provides a reality check but they also can be used to expose the weaknesses and strengths of doing simulations. The lessons learned from this research will hopefully lead to better designed and executed simulations in the future. Like laboratory experimentation, simulation is another tool in the scientist's toolkit of ways to apply the scientific method to a problem. For the same reasons why one would compare microscopy observations to calorimetry measurements, simulations should always be performed in the context of other experiments and simulations.

1.4 Other Work

What is presented in this thesis are projects that were carried to completion. Like most research efforts, there are other projects that are yet to be finished. Much of what was learned from these projects has been immensely useful and has been applied to the work contained here. A brief reflection on this doctoral career follows.

The process of finding a research topic began with an interest in liquid crystals. Polymer-dispersed liquid crystals (PDLC's), in particular, was a relatively new field and the need to understand PDLC's became pressing as a result of new applications for video displays and shutters. PDLC's are droplets of liquid crystals dispersed in a polymer matrix. Products made with PDLC's have the advantages of being leak-proof, flexible, and memory-retaining. They can be switched on and off via an electric field. The original project was to simulate, first in two dimensions and then in three, liquid crystal droplets in an alternating field to measure the switching speed. It was soon realized that some of the more fundamental questions regarding liquid crystals have not yet been answered satisfactorily so the goals of the projects changed and the results form the basis of chapter 2. Through the work in chapter 2, we now have a good understanding of the effects of elastic moduli, temperature, field, and surfaces on liquid crystals.

Near the end of that project, contact was made with Thomas's research group at MIT. They had published experimental measurements on the shrinkage of inversion wall loops. Since the liquid crystal program only needed a slight modification to simulation inversion wall loops, the relevant simulations were performed and indeed the results agreed with the experimental data. During this time, the desire to simulate liquid crystals in three dimensions grew and the outcome was a series of evolutionary steps toward acquiring an in-house set of 3-D graphics capabilities. Besides writing a new program to simulate and display liquid crystals in 3-D, two other programs were written, one which simulated the deposition of atoms onto a surface, for example in chemical vapor deposition, and another which placed random charges in a plane and allowed them to attract and annihilate. The results from the latter program are directly analogous to the liquid crystal defect annihilation problem and will be discussed in chapter 2 as well.

After the simulations on liquid crystals came to a close, attention turned to applying molecular dynamics to a range of problems in polymer physics. Because there were so many potential projects that could use molecular dynamics, an idea was spawned of writing one program that could handle all the required chain architectures, environmental conditions, and data analyses. Out of this effort came the program Usim, or the universal molecular simulator. Over the last several years it has been used on a wide range of problems.

The first task was to test and benchmark the program. This was done with two simulations, one which measured the diffusion coefficient of a single chain, and the other which determined the scaling of the radius of gyration versus chain length for the excluded-volume condition. Both results agreed with theory.

Usim has been used to study polyelectrolytes. In one set of simulations, a charged rod was fixed in space and counterions were allowed to float within a certain range from the rod. The counterion density versus distance from the rod was plotted to look for counterion condensation. Preliminary data suggest that counterion condensation is not a first order transition. The potential as distance from the rod was also plotted. In another set of simulations, we tested the hypothesis that under certain conditions, polyelectrolytes might be attractive and form aggregates. It was found that at low temperatures, positive and negative ions may associate into strings of alternating charges which link polyelectroytes together, but it is unclear that experimentally this would occur before the solution freezes.

Surfactants are related to polyelectrolytes. One original project was to simulate micelles, rod-like micelles, branched micelles, and lipids, and to eventually simulate molecular transport across a lipid bilayer. It was soon realized that these systems require exceedingly large number of molecules to produce a good simulation and the computing power available to us was not enough for this. Nevertheless, all

these structures were produced on a smaller scale, demonstrating the usefulness and flexibility of the program.

Usim has also been used to study polymer brushes. The density profiles of polymer and polyelectrolyte brushes under various salt concentrations were plotted, agreeing with Monte Carlo and theoretical results published by Friedel von Goeler [13].

Other molecular architectures simulated by Usim include stars, dendrimers, and block copolymers. Using Usim, we were able to reproduce lamellar and spherical morphologies for diblock copolymers. Radial density profiles for dendrimers successfully matched those obtained from Monte Carlo simulations performed by Paul Welch [14].

The main use of Usim, however, has been for polymer crystallization, covered in chapter 4. Additional studies on crystallization of branched polymers have been performed but not reported. Results indicate the melting point depression and lower degree of crystallization associated with increased branch content. One question answered by a recent experiment by Yvonne Akpalu was whether the side chains are included in or excluded from the lamella [15]. Our simulation has shown that short branches are excluded while long ones approaching the thickness of the lamella may be included.

1.5 Closing Remarks

We hope that this chapter has introduced the reader to the motivation behind the work, the major concepts involved, and the logical subdivisions of the work, and has provided the roadmap of this research depicting the paths chosen and the many possible branches and detours that were and were not made. In Chapter 5

where the dissertation is summarized, suggestions for future work will draw upon some of the themes covered in this chapter.

We now proceed to the first major topic: liquid crystal defect annihilation.

CHAPTER 2

ANNIHILATION KINETICS OF LIQUID CRYSTAL DEFECTS

2.1 Introduction

Liquid crystalline states of small molecules are inherently dynamic due to the relatively small energies required to perturb them. This characteristic is being exploited in technological areas such as displays and shutters, by controlling different conditions such as temperature, external orienting fields, geometry, and elastic anisotropy inherent to the system. [16] When a system containing liquid crystals is quenched from the isotropic to nematic state, topological defects called disclinations are created spontaneously. These defects are unstable and evolve with time since the quench. The study of topological defects has played an important role in the physics of liquid crystals[17–19]. Topological defects arise in many other areas of physics such as fluid to solid phase transitions[20], vortex lines in superfluids[21], and cosmology[22].

In two dimensions ($d = 2$), each of the various defects can be assigned a strength and a sign, and may be treated as a charge. Oppositely signed defects attract with a potential proportional to the inverse of separation distance between them and annihilate. Similarly signed defects repel and push the partners toward oppositely signed defects for eventual annihilation. Consequently, the number of defects in the

system decreases with time. In three dimensions ($d = 3$), the disclinations exist as lines or strings. During coarsening, disclination line density decreases. The process of evolution of defects with time occurs in both two and three dimensions via a highly cooperative pathway mediated by the anisotropic elastic medium. This coarsening process is controlled by both the elastic and Brownian forces. The primary objective of this chapter is to describe the details of evolution of defect annihilation under the influence of prescribed elastic anisotropy, external fields and physical boundaries, in both two and three dimensions.

The ordering dynamics in liquid crystalline systems has been extensively investigated experimentally[2, 23–38]. The general result is that the defect density $\rho(t)$ decreases with time t, since the quench from disordered to ordered state, as a power law,

$$\rho(t) \sim t^{-\nu}. \tag{1}$$

In most of these experiments, ν is less than 1. There have also been many recent theoretical and numerical studies[39–54] of defect dynamics reporting different values of ν. In view of the analogy between the defects and charges, the numerical studies in two dimensions have treated the defects to be point-like + and − charges. In general, the defect density $\rho(t)$ at time t is found to scale as $t^{-\nu}$. Several different values of ν have been reported in the literature. If we consider the mean field argument that the rate with which ρ changes is proportional to the probability of binary collisions,

$$\frac{d\rho}{dt} \sim -\rho^2, \tag{2}$$

then $\nu = 1$, on dimensional grounds. Nevertheless this mean field result is not observed in simulations. The above mean field argument treats the system as consisting of isolated pairs of defects at random separation distances. In reality,

isolated pairs are rare; each defect is surrounded by a host of other defects, some with positive and some with negative sign. Therefore, the path two defects follow to annihilation may not be a simple straight line drawn between the pair but rather tortuous. The process is further complicated by the simultaneous movements of all defects, thus constantly changing the background forces that affect any pair of defects. The effect of such a collective motion is to slow the process, leading to a power law exponent that is smaller in magnitude from the mean field value.

Toussaint and Wilczek[39] studied the pure diffusive regime of annihilation kinetics of a $d = 2$ system with + and − point-like defects, which annihilate on contact but do not otherwise interact. They showed that $\nu = 0.5$ for this system. Mondello and Goldenfeld[47], by analyzing the XY model with continuous-symmetry conserved order parameter at zero temperature, suggested that in the non-diffusive regime with long-range logarithmic potential between defects in $d = 2, \nu = 0.75$. Yurke *et al.*[50] considered the same system and showed that

$$\rho(t) \sim t^{-\nu} \ \ ln\ t, \ \ \nu = 1, \tag{3}$$

by accounting for the dependence of drag mobility of defects on the defect density. Jang *et al.*[54] numerically studied the dynamic evolution of a $d = 2$ system of charged particles which interact with a logarithmic potential and annihilate on contact with an opposite charge. The particles were allowed to move with constant mobility. They recovered the diffusive regime result, $\nu = 0.5$, at high temperatures where Brownian motion dominates. In the limit of the deterministic regime where interparticle forces dominate the dynamics, they found $\nu = 0.90 \pm 0.05$. To explain this new result, they suggested a simple scaling hypothesis where $\nu = 6/7$ for $d = 2$.

We have performed Monte Carlo simulations of defect annihilation in both $d = 2$ and 3, using the Frank free energy[17, 18]. We have considered explicitly the

roles of elastic anisotropy, surface anchoring and external fields on the kinetics of annihilation of defects. Our numerical results are consistent with those of Jang *et al.* in $d = 2$. By generalizing the scaling hypothesis of Jang *et al.*[54], we find that ν is given by

$$\nu = \frac{d(d+1)}{(d^2+2d-1)}, \tag{4}$$

where d is the space dimension. ν is 6/7 for both $d = 2$ and 3 and this result is supported by the numerical data presented below.

We also find that the value of ν is independent of the ratio of the splay elastic constant to the bend elastic constant in two dimensions. Furthermore we report below that the number of defects near the surface boundaries at intermediate times is higher for intermediate strengths of surface anchoring.

The coarsening of defects in a system with an external field follows a different law from the above. Pargellis *et al.*[35] showed that, when the aligning field couples to the director field via a dipole interaction, the defect density decays exponentially with time,

$$\rho(t) = \rho(0) \;\; exp(-\Gamma t), \tag{5}$$

where Γ is the decay rate. This law arises from the argument that the time for annihilation of defect pairs in an orienting field is proportional to separation distance within each pair and that the probability distribution of separation distances is exponential. The simulation data presented below support this law and Γ is found to increase with the strength of the aligning field.

2.2 Scaling

We present here a generalization of the original scaling argument by Jang, *et al* [54]. Consider a large region of characteristic size L in d dimensions. Let us now divide this region into small cells of volume ℓ^d where ℓ is the average distance between defects in the initial stage, so that the initial density ρ_0 of defects is $\rho_0 \sim \ell^{-d}$. The number of defects at the surface of the region of size L is proportional to $\rho_0 \ell L^{d-1}$. The fluctuation in this number is proportional to $(\rho_0 \ell L^{d-1})^{\frac{1}{2}}$. Assuming that the fluctuation in the net charge in the region of size L is proportional to the fluctuation in the number of defects at the surface of the region, the defect density fluctuation $\delta\rho_0(L)$ is proportional to $(\rho_0 \ell L^{d-1})^{\frac{1}{2}} L^{-d}$,

$$\delta\rho_0(L) \sim (\rho_0 \ell)^{\frac{1}{2}} L^{-\frac{(d+1)}{2}}. \tag{6}$$

According to the scaling hypothesis, when all defects of opposite sign in volume L^d have annihilated, defect density at this moment is comparable to $\delta\rho_0(L)$. We therefore assume that in the scaling regime, the defect density $\rho(t)$ is given by Eq.(6),

$$\rho(t) \sim (\rho_0 \ell)^{\frac{1}{2}} L^{-\frac{(d+1)}{2}}(t). \tag{7}$$

In the deterministic regime, by ignoring the thermal noise and inertial force, the dynamics of a labeled defect is approximated by the equation of motion,

$$\zeta \frac{d\mathbf{r}}{dt} = \mathbf{F} \tag{8}$$

where $\mathbf{r}$ is the position of the defect, ζ is the friction coefficient of the defect against the medium, and $\mathbf{F}$ is the force acting on the defect due to other defects. If R is the average spacing between the defects, the force scales as

$$F \sim R^{(1-d)} \sim \rho^{\frac{(d-1)}{d}} \tag{9}$$

since $\rho \sim R^{-d}$. Substituting Eq.(7) into Eq.(9), the force scales with the time-dependent L as

$$F \sim (\rho_0 \ell)^{\frac{(d-1)}{2d}} L^{-\frac{(d^2-1)}{2d}}. \tag{10}$$

Combining this result with the balance of frictional and potential forces given by Eq. (8), we obtain the scaling form,

$$L(t) \sim (\rho_0 \ell)^{\frac{d-1}{d^2+2d-1}} \quad t^{\frac{2d}{d^2+2d-1}} \tag{11}$$

Substitution of Eq.(11) in Eq.(7) yields,

$$\rho(t) \sim (\rho_0 \ell)^{\frac{d}{d^2+2d-1}} \quad t^{-\nu}, \tag{12a}$$

where

$$\nu = \frac{d(d+1)}{(d^2+2d-1)}. \tag{12b}$$

The mean field result of $\nu = 1$ is recovered for $d = 1$ and $d = \infty$. For both $d = 2$ and 3, ν is $\frac{6}{7} \simeq 0.8571$.

2.3 Simulation Method

The system is discretized into lattice sites. In two and three dimensions there are N^2 and N^3 sites, respectively. In an initial configuration of liquid crystals each of these sites is randomly assigned an orientation $\vec{n}$ for the director of the volume element representing the particular site. Based on the orientation of the director at all sites, we compute the total free energy F of the system as given by the Frank free energy,

$$\begin{aligned} F &= \frac{1}{2}\int dV\{k_{11}(\nabla \cdot \vec{n})^2 + k_{22}(\vec{n} \cdot \nabla \times \vec{n})^2 + k_{33}(\vec{n} \times \nabla \times \vec{n})^2\} - \qquad (2.1) \\ &\quad \frac{1}{2}\int dV(\vec{H} \cdot \vec{n})^2 + \frac{1}{2}\int dS(W \sin^2\phi) \qquad (2.2) \end{aligned}$$

where K_{11}, K_{22}, and K_{33} are the splay, twist, and bend elastic constants. $\vec{X}$ is the generalized external field given by

$$\vec{X} = \sqrt{\Delta\epsilon\ \epsilon_o}\ \vec{E} + \sqrt{\frac{\Delta\chi}{\mu_o}}\ \vec{B} \tag{2.3}$$

where $\vec{E}$ is the electric field, $\vec{B}$ is the magnetic field, $\Delta\epsilon$ and $\Delta\chi$ are the electric and magnetic susceptibilities, and ϵ_o and μ_o are the permittivity and permeability of vacuum. W is the strength of the anchoring interaction of liquid crystals at the interface with the boundaries of the system. ϕ is the deviation of the angle of orientation of the director away from the preferred orientation at the interface. Preferred parallel and perpendicular alignments of liquid crystal at interfaces are considered. $\int dV$ denotes the volume integration while $\int dS$ denotes integration over the interfaces making the physical boundaries of the system. The boundary condition is imposed by representing the bounding surfaces as a fixed set of directors interacting with the liquid crystal directors via the surface interaction term. Therefore the various parameters are the elastic constants K_{11}, K_{22}, and K_{33}, strength of the external field X and the anchoring strength W. In two dimensions, K_{22} is zero as twist is not allowed. Since the probability of realizing a particular director field is given by the Boltzmann weight exp $(-F/T)$, the reduced temperature T (in units of the Boltzmann constant being unity) is also a parameter.

After computing the free energy of the initial configuration, the system is allowed to evolve for the chosen values of the various parameters. The evolution is carried out in the following manner. In one unit of time, each lattice site is selected and the director at each site is rotated by a small angle θ, usually 2 degrees. It is extremely important to choose a small enough angle for the rotation of the director in order to obtain reliable simulation data. If small enough angles are not cho-

sen, the results will be dependent on the choice of the mesh size in angle. Figure 2.1 shows the power law exponent as a function of the step size, expressed as the minimum angle of rotation per site per time step.

The free energy of each site associated with the new orientation is computed from the director orientations of its four (six) nearest neighbors in two (three) dimensions. If the total free energy F_n of the new configuration is less than the old value F_o, then the new configuration is accepted. Otherwise we employ the Metropolis algorithm whereby the new configuration is accepted if $exp((F_n - F_o)/T) > \eta$ where η is a random number in the interval [0,1]. At the end of each time step, the director field, the number and nature of defects, and the total free energy are recorded. In two dimensions, the defects are identified as follows. About every lattice site, there are four cells each containing a director. With respect to a chosen director, we calculate the sum of four angular differences between successive pairs of directors, as we go around the site clockwise from the chosen director. If the sum is a multiple of π, there is a defect. The value of the multiple gives the nature of the defect. In three dimensions we count the number of lattice sites with free energy greater than a certain cutoff value. This number is taken as the disclination line length. In our simulations the cutoff is taken to be unity. The above procedure is continued until necessary information is accumulated. The various averages are constructed by averaging over about 50 independent simulations for the same set of values of parameters.

2.4 Results and discussion

The simplest system corresponds to the situation of equal elastic constants without any external fields at temperatures where the liquid crystals are in the

nematic state. The number of defects versus time is plotted double logarithmically in Fig. 2.2. The data are obtained from two dimensional simulations on 100^2 lattices with periodic boundary conditions for $K_{11} = 1 = K_{33}, T = 0.2$ and $K_{22} = 0 = X$. The data presented in Fig. 2.2 are the averages over 100 independent simulations. There are two distinct regimes as seen in the figure. The early regime corresponds to an exponential decay of defect density with time representing very early local annihilation. We will not be concerned with this early regime. For long times, we observe that $\nu = 0.84 \pm 0.03$. This result is consistent with the earlier simulation result of $\nu = 0.90 \pm 0.05$ by Jang *et al.*[54]

Before we proceed to address the effects of temperature and other physical parameters on the time dependence of defect density, we comment on finite size effects on the reported results. In two dimensions we have carried out the simulations on lattices of size N^2 with $N = 25, 50, 100, 200$, and 500. Visual observation of any typical configuration of defects shows that each defect influences an area of about 15^2 for the above values of the parameters. The same value of $\nu = 0.84 \pm 0.03$ is observed asymptotically for all lattices with $N \geq 50$. In view of this, we have studied lattices of convenient size of 100^2. The data given below correspond to this lattice size.

2.4.1 Effect of Temperature

Similar to the data of Fig. 2.2, simulation results on a square lattice of linear size $N = 100$ with periodic boundary conditions were collected at different reduced temperatures in the range of T from 0.01 to 0.6 for $K_{11} = 1 = K_{33}$ and $X = 0$. At each temperature, the results were averaged over at least 50 independent simulations. The values of the exponent ν extracted from plots of these data, as in

Fig. 2.2, in the long time regime are plotted versus the reduced temperature T in Fig. 2.3 for $K_{11} = 1 = K_{33}, X = 0$, and $N = 100$.

It is clear from Fig. 2.3 that there is a wide temperature range in which ν is between 0.8 and 0.85. It is therefore not surprising that many experiments and simulations under different conditions have reported the same power law. The lowest temperature we have studied is 0.01, and the simulation results are not reliable at temperatures lower than 0.01 due to poor acceptance ratio in the Metropolis sampling procedure.

At higher temperatures, the potential elastic interaction becomes insignificant and the Brownian forces dominate. Therefore we expect to approach the diffusive regime where $\nu = 0.5$ at such higher temperatures. We indeed find ν to be smaller than 0.5 due to the additional spontaneous generation of defects originating from large fluctuations at higher temperatures.

2.4.2 Effect of Elastic Moduli Ratio

The asymptotic result of Eq. (3) in the scaling regime is universal and is expected to be independent of the details of the various elastic constants. In order to verify this, we have performed simulations for different values of the elastic moduli ratio $K_r = K_{11}/K_{33}$. Furthermore, we need to add the constraint that the sum of the elastic constants be a constant, because a system with K_{11} and K_{33} of 4 and 2, respectively, is different from a system with K_{11} and K_{33} of 2 and 1. By arbitrarily setting the average of the elastic constants to be 1, K_{11} and K_{33} are given by $K_{11} = 2K_r/(1 + K_r)$ and $K_{33} = 2/(1 + K_r)$. Simulations were carried out on a square lattice with periodic boundary conditions for K_r ranging from 10^{-2} to 10^2 at the reduced temperature of 0.2. The asymptotic decay law is the same as

in Fig. 1 and the resulting exponent is plotted in Fig. 3 against K_r. It is seen that the value of ν is independent of K_r at low temperatures. This is in agreement with experimental data which show the same value of ν regardless of the chemical composition of the liquid crystals. It is to be pointed out that it is essential to choose very small step sizes (of the order of two degrees) in the angle of rotation in our Monte Carlo simulations. If sufficiently small step sizes are not used, spurious dependencies of ν on K_r will be obtained.

2.4.3 Effect of Surface Anchoring Energy

In this section we report simulation data for different values of the surface anchoring energy W in the range from 0 to 2.5 corresponding respectively to the free surface boundary and the rigidly anchored surface. In these simulations, we considered relatively small droplets of linear size $N = 30$, which are small enough to capture the surface effects but not so small as to be comparable to the size of a single defect. The simulations were carried out at the reduced temperature $T = 0.03$ and $K_{11} = 1 = K_{33}$. For each value of W, the data were averaged over 100 independent simulations. The resulting data were analyzed by making plots of the relative number of defects in the droplet as compared to the free boundary case, as shown in Fig. 4. Each curve in Fig. 4 shows the excess number of defects at a particular time step as a function of W. The figure shows that the excess number of defects generally decreases over time, as expected. It also shows that the number of defects is lowest for the droplets with no surface anchoring energy. This happens because the defects are not constrained by the surface and can disappear by moving into the free interface instead of finding an opposite defect to annihilate with.

The shape of the curves in Fig. 4 can be qualitatively understood by considering the effect of the interface on the motion of a nearby defect. Typical configurations of defects for $W = 0, 0.5, 1$, and 2 at the time step of 1000 units are shown in Fig. 5. When surface anchoring energy is low (Fig. 5a), the surface does not present a barrier to the rotation of liquid crystals. Hence it is energetically favorable and possible for defects to simply move out of the droplet. At intermediate surface anchoring energies (Fig. 5b), the constraint posed by the surface anchoring is sufficient to prevent defects from escaping the droplet and the rotational flexibility is still sufficient so that defects linger near the surface. At high surface anchoring energies (Fig. 5c and 5d), the surface is so rigid that it cannot accommodate the distortions of director field associated with defects. Consequently defects are now pushed away from the surface into the interior of the droplet. With this in mind, the curve on Fig. 4 for the time of 2000 units correctly shows a maximum at intermediate surface anchoring energies. In Fig. 5, we observe that the snapshot at $W = 0.5$ shows the most defects. It is to be noted that the snapshots of Fig. 5 are for only one of 100 independent simulations whereas the results of Fig. 4 are the averages over these 100 simulations.

2.4.4 Effect of Field Strength

The presence of an orienting external field is expected to significantly affect the pathway of annihilation of defects. In the absence of external fields, the defects are randomly distributed at early times and each defect interacts with a large number of nearby defects. On the other hand, in the presence of an orienting field, + and – defects pair up and proceed to annihilate. This difference is illustrated in Figs. 6a and 6b where simulated cross-polars are presented for the presence and

absence of external field respectively. The data in Fig. 6 are for two dimensions with $N = 100, T = 0.1, K_{11} = 1 = K_{33}, W = 0$ and $X = 0.3$ and 0 at the time step of 1000 units. For the same values of N, T, W, K_{11}, and K_{33}, we have performed simulations for different strengths of the external field variable X in the range from 0 to 1. The number of defects, averaged over 50 independent simulations, is plotted semi-log in Fig. 7 against time step. The figure clearly shows that the number of defects for systems with an orienting field indeed decreases exponentially with time at long times, in agreement with Eq. (5). The decay rate Γ obtained from the curves of Fig. 7 is found to increase with the strength of the external field X, as demonstrated in Fig. 8.

2.4.5 Three Dimensional Systems

The simulation method is the same as the one used above for two dimensional systems. Differences include the consideration of six instead of four nearest neighbors and the addition of the twist elastic modulus K_{22}. In three dimensions, disclinations exist as lines or strings. We have estimated the disclination line density by recognizing that lattice sites along the disclinations have high energies. Therefore the disclination line density is expressed as the number of lattice sites where the elastic energy is above a certain cutoff value. We have taken this cutoff value to be 1. A typical configuration of the disclinations in three dimensions is given in Fig. 9 corresponding to $N = 70, T = 0.04, K_{11} = K_{22} = K_{33} = 1, X = 0 = W$ at the time step of 6349 units. The time evolution of the number of sites along various disclinations in a three dimensional lattice of linear size $N = 70$ with periodic boundary conditions and $T = 0.01, K_{11} = K_{22} = K_{33} = 1, X = 0$ and $W = 0$ is presented in Fig 2.11 for a typical case. The value of ν for this particular simulation is 0.86.

Upon averaging over five independent simulations, the value of the exponent ν in the asymptotic regime is 0.88 ± 0.05 and is in excellent agreement with the scaling prediction of Eq. (4). Since this result is consistent with other simulations[51] reported in the literature, we do not provide additional data from three dimensional simulations.

2.5 Conclusion

We have derived an expression for the decay exponent ν based on scaling arguments of Jang *et al.*[54] as a function of space dimension, given by Eq. (4). In both two and three dimensions, ν is 6/7 and our simulation results support this result. Our simulations of the dynamics of defects in liquid crystalline systems use the full Frank free energy including elastic anisotropy, surface anchoring and applied fields. The numerical result of 0.85 ± 0.03 for ν obtained in our simulations in two dimensions is universal across a wide range of temperature and elastic moduli ratio. The same value of the exponent is found in our three dimensional simulations as well.

The surface anchoring has been found to play a non-universal role on the defect density in the vicinity of interfaces at the boundaries of liquid crystalline domains. Moderate anchoring strengths exhibit a trapping effect on the defects while strong anchoring repels defects away from the interface. In the presence of an external orienting field, the defect density decays exponentially with time and the decay rate is found to increase with the strength of the external field.

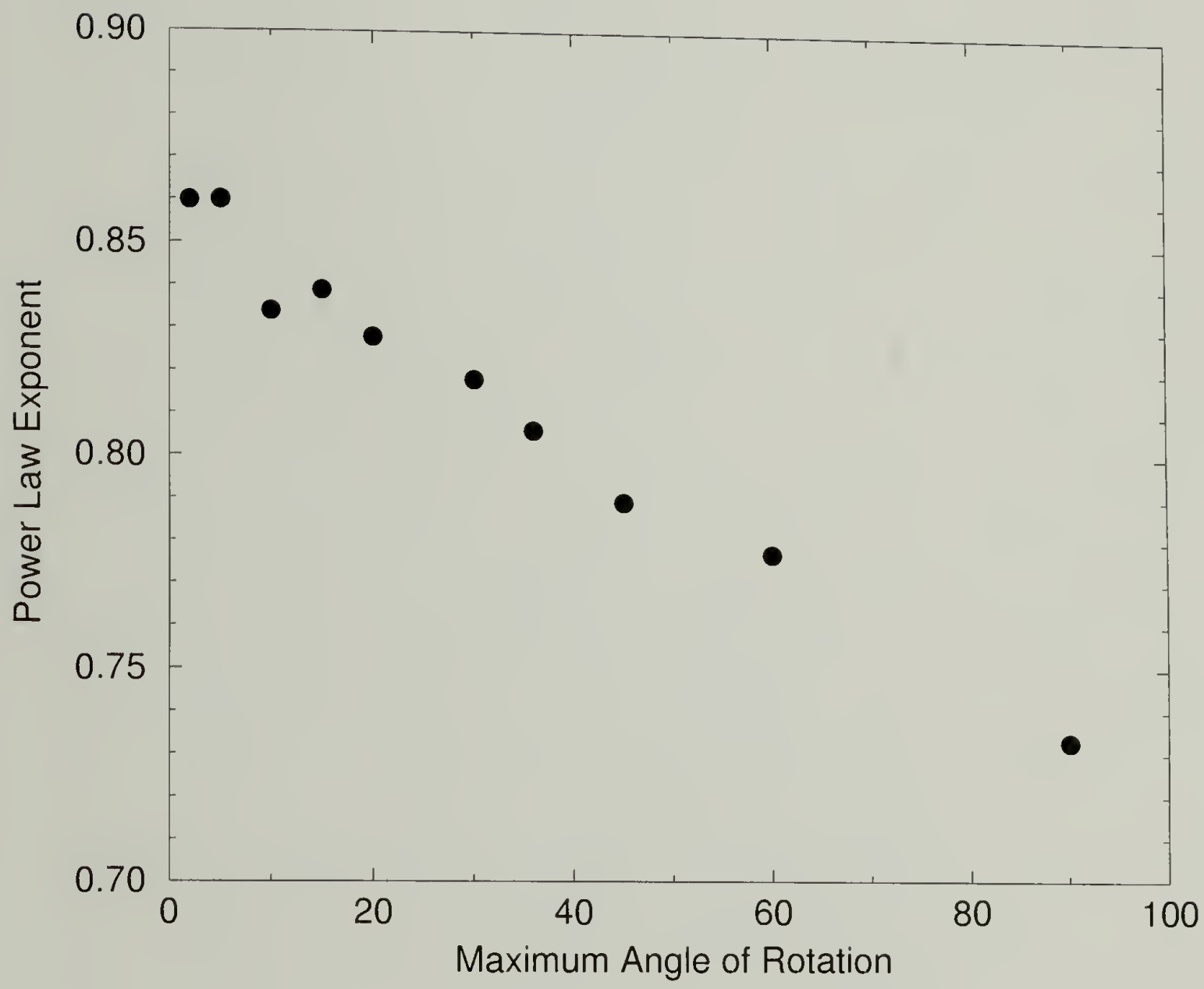

Figure 2.1 The measured power law exponent is a function of the maximum Monte Carlo step size per iteration, showing the importance of choosing a small step size to obtain accurate results. Data points represent average over 100 runs, at $T = 0.1$ on a 100^2 lattice.

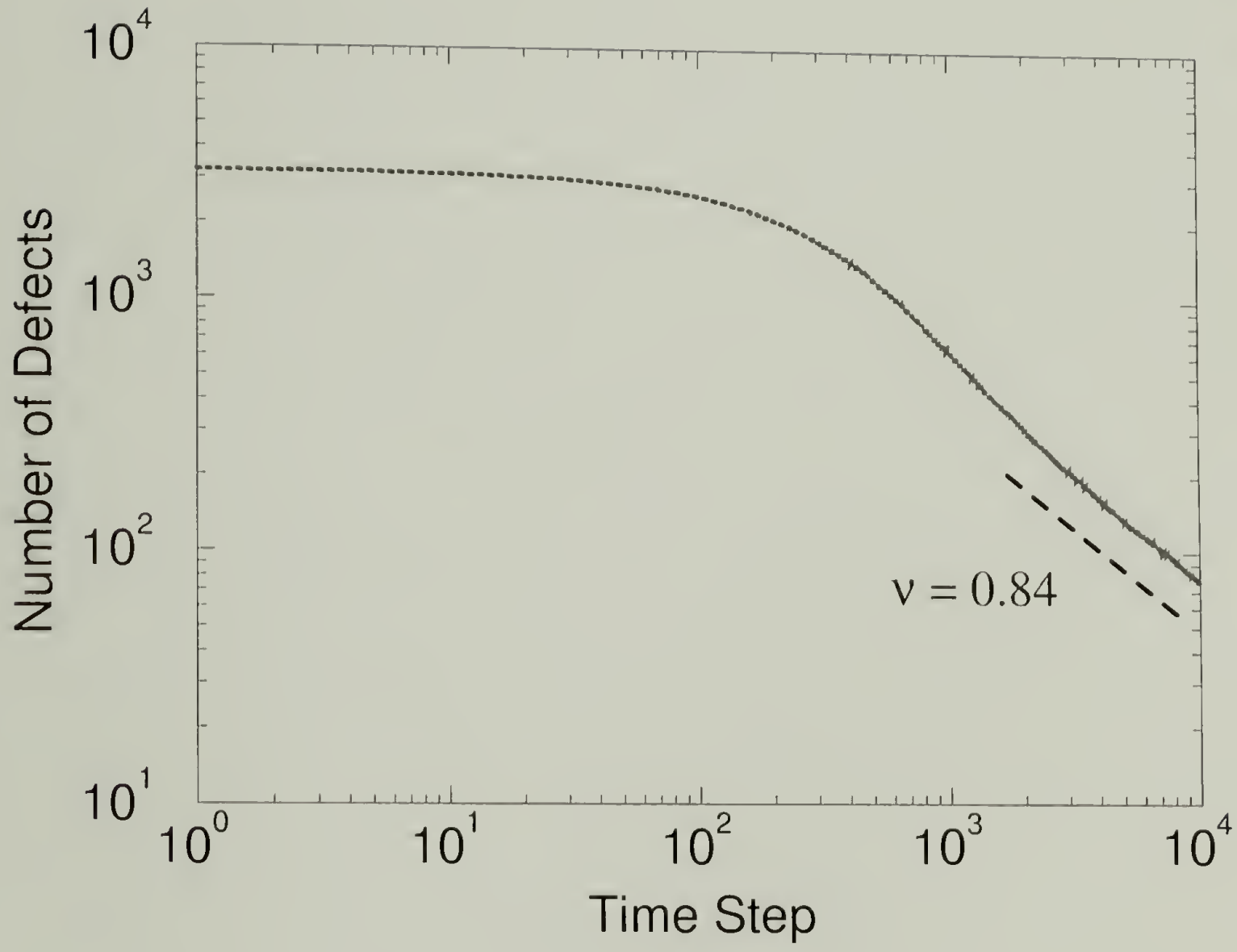

Figure 2.2 Double logarithmic plot of number of defects versus time step, showing asymptotic scaling behavior of $\nu = 0.84$, for $N = 100, K_{11} = 1 = K_{33}, T = 0.2, X = 0$ on two dimensional lattices with periodic boundary condition.

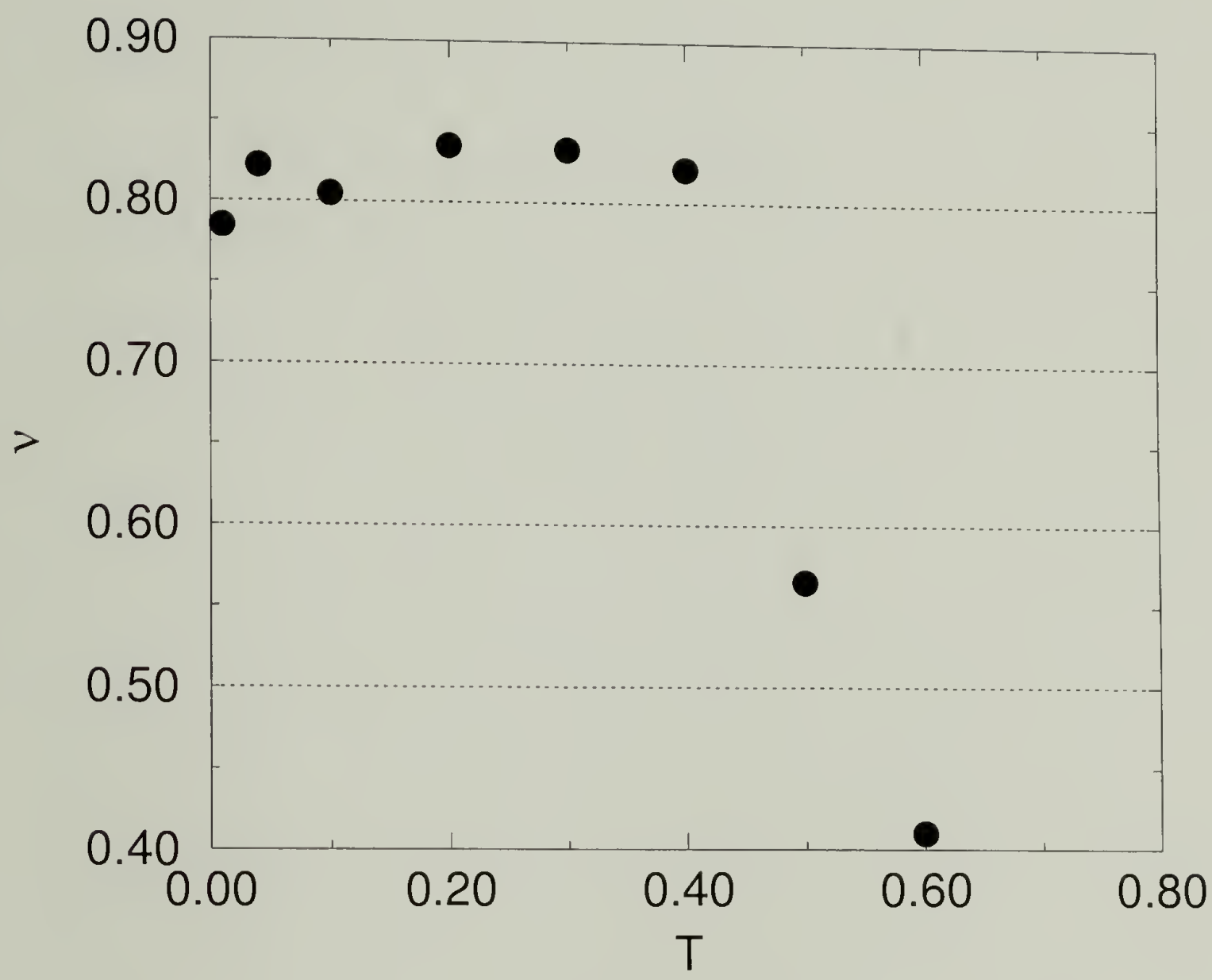

Figure 2.3 ν is constant over a wide temperature range and drops off when Brownian forces dominate over interparticle forces. ($N = 100, K_{11} = 1 = K_{33}, X = 0 = W$)

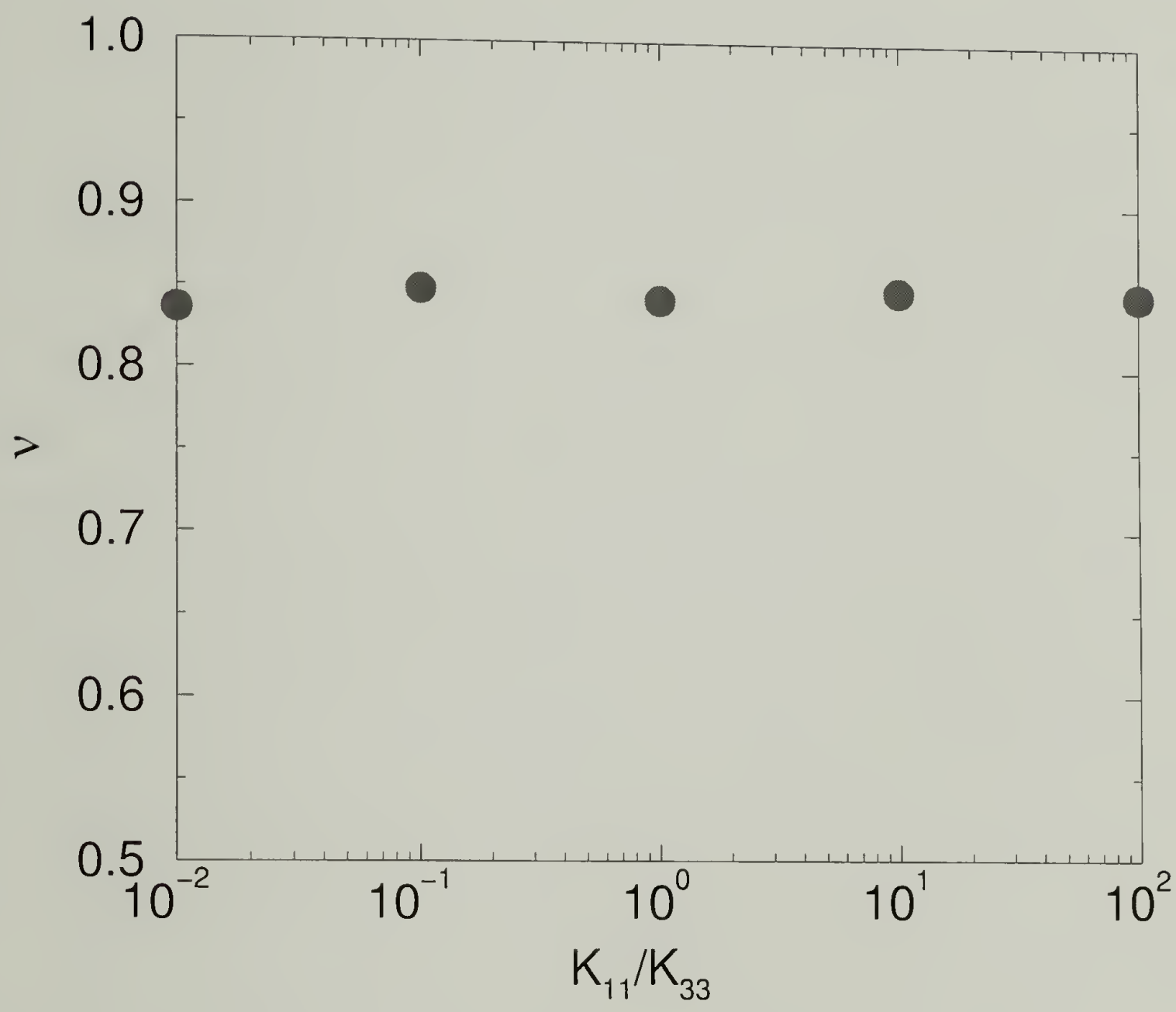

Figure 2.4 ν is independent of the ratio of the splay to bend elastic moduli. $(N = 100, T = 0.2, X = 0 = W)$

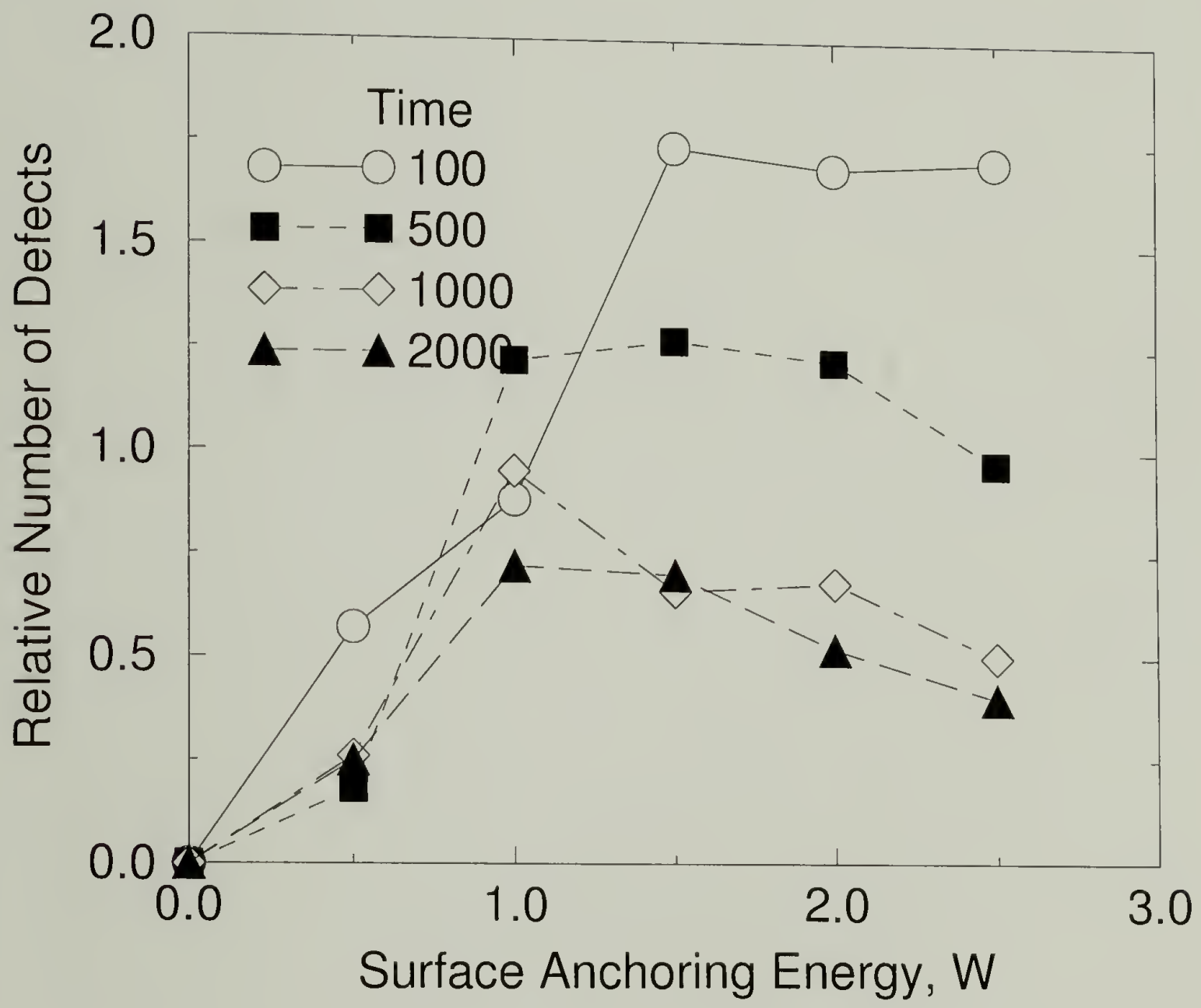

Figure 2.5 Effect of surface anchoring strength on number of defects in a circular droplet. Each curve shows, at selected time steps, the relative number of defects for W ranging from 0 to 2.5 compared to the number of defects at $W = 0$. ($N = 100, K_{11} = 1 = K_{33}, T = 0.03, X = 0$)

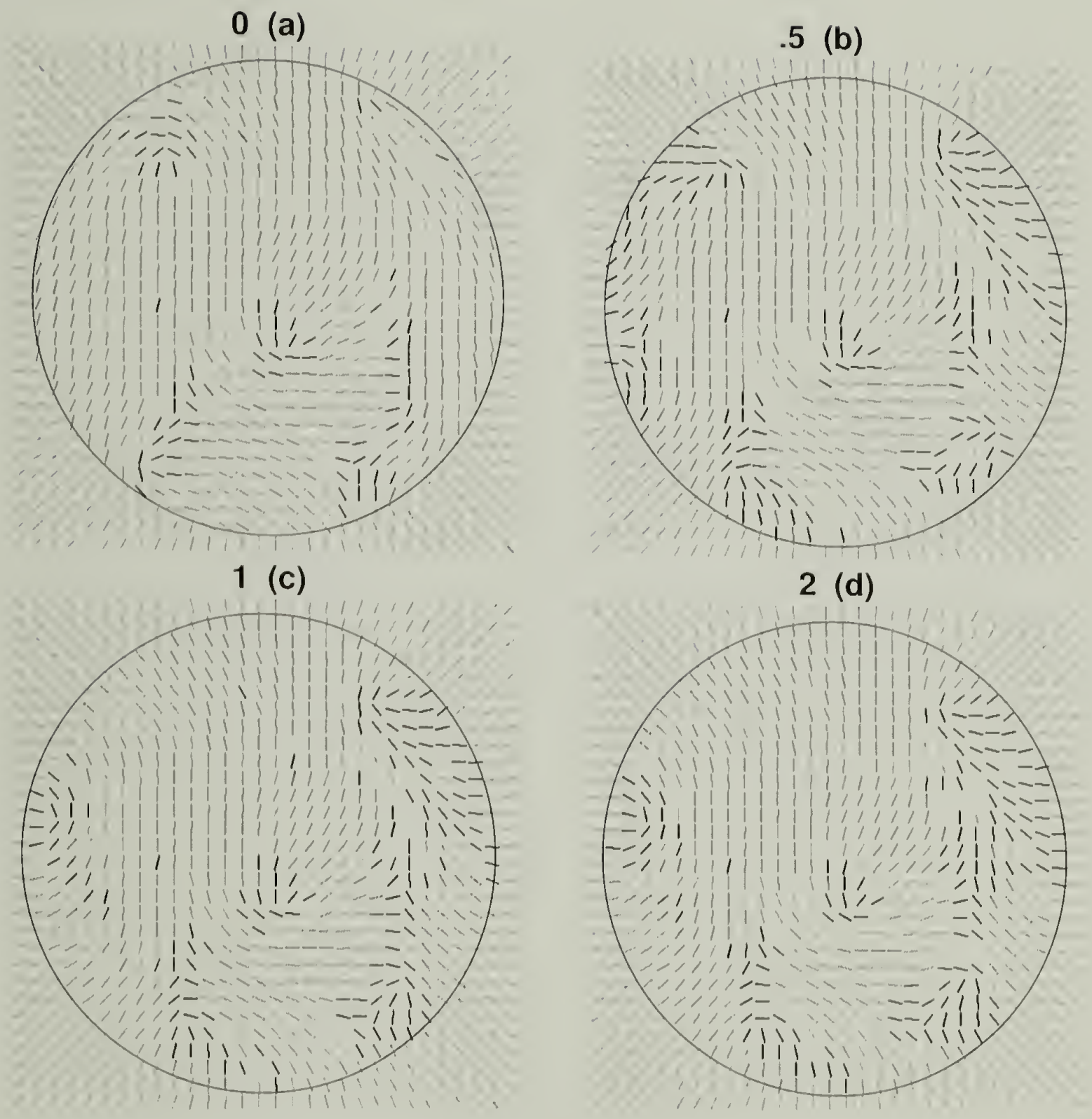

Figure 2.6 Snapshots taken at time step = 1000, from the same initial configuration, for $W = 0, 0.5, 1$, and 2 in $(a), (b), (c)$, and (d) respectively. Circle shows boundary of the droplet. Conditions are the same as in Fig. 2.5

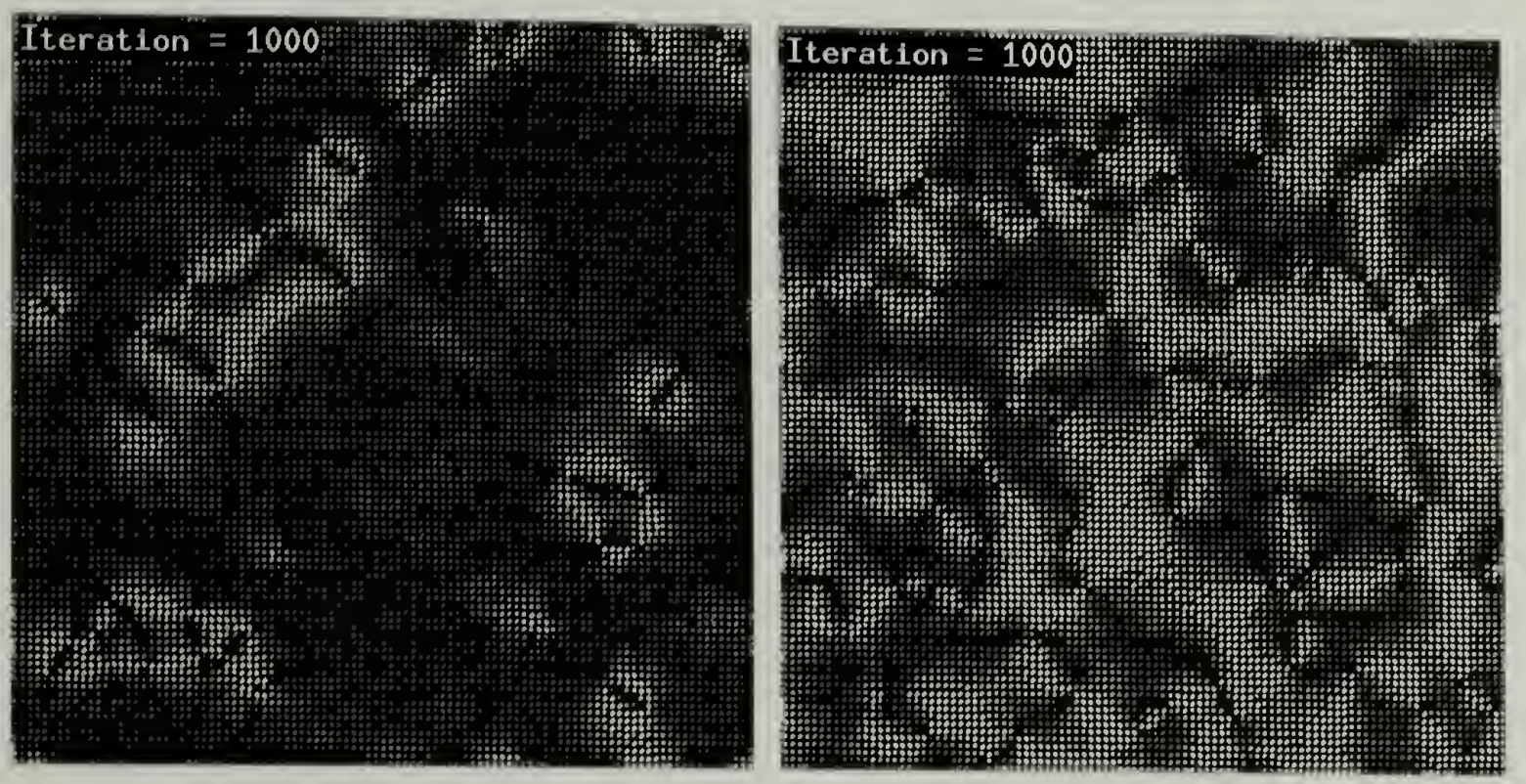

(a) (b)

Figure 2.7 Comparison of simulated cross-polar images with (a) and without (b) an external field. (a) shows mostly isolated defect pairs while (b) shows typical schlieren pattern. The field is along the horizontal direction. ($N = 100, K_{11} = 1 = K_{33}, T = 0.01, W = 0, X = 0.3$ and 0)

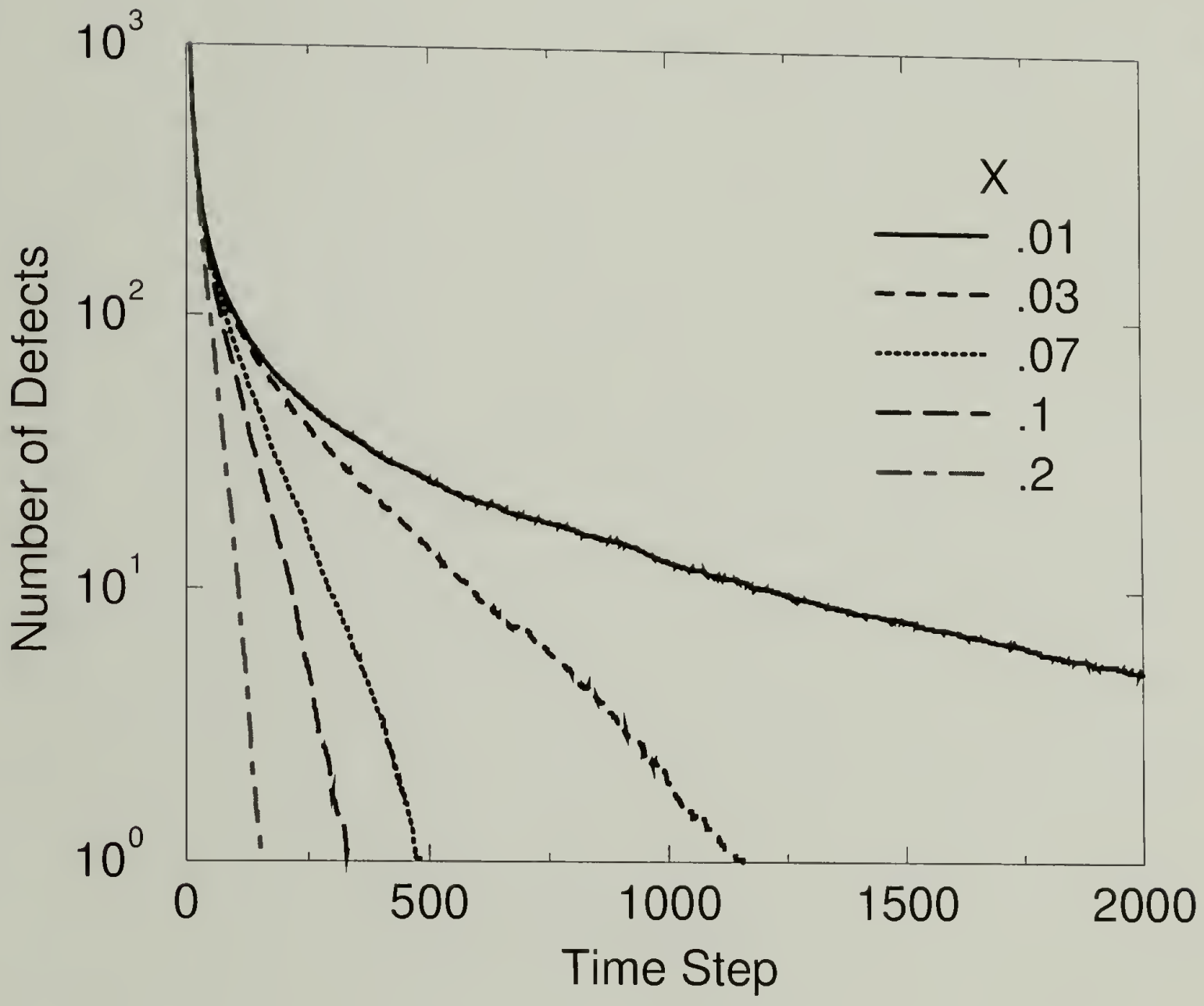

Figure 2.8 Defect density decays exponentially with time in the presence of external field. Semilog plot of number of defects versus time step for $X = 0.01, 0.03, 0.7, 0.1$, and 0.2. $(N = 100, K_{11} = 1 = K_{33}, T = 0.1, W = 0)$

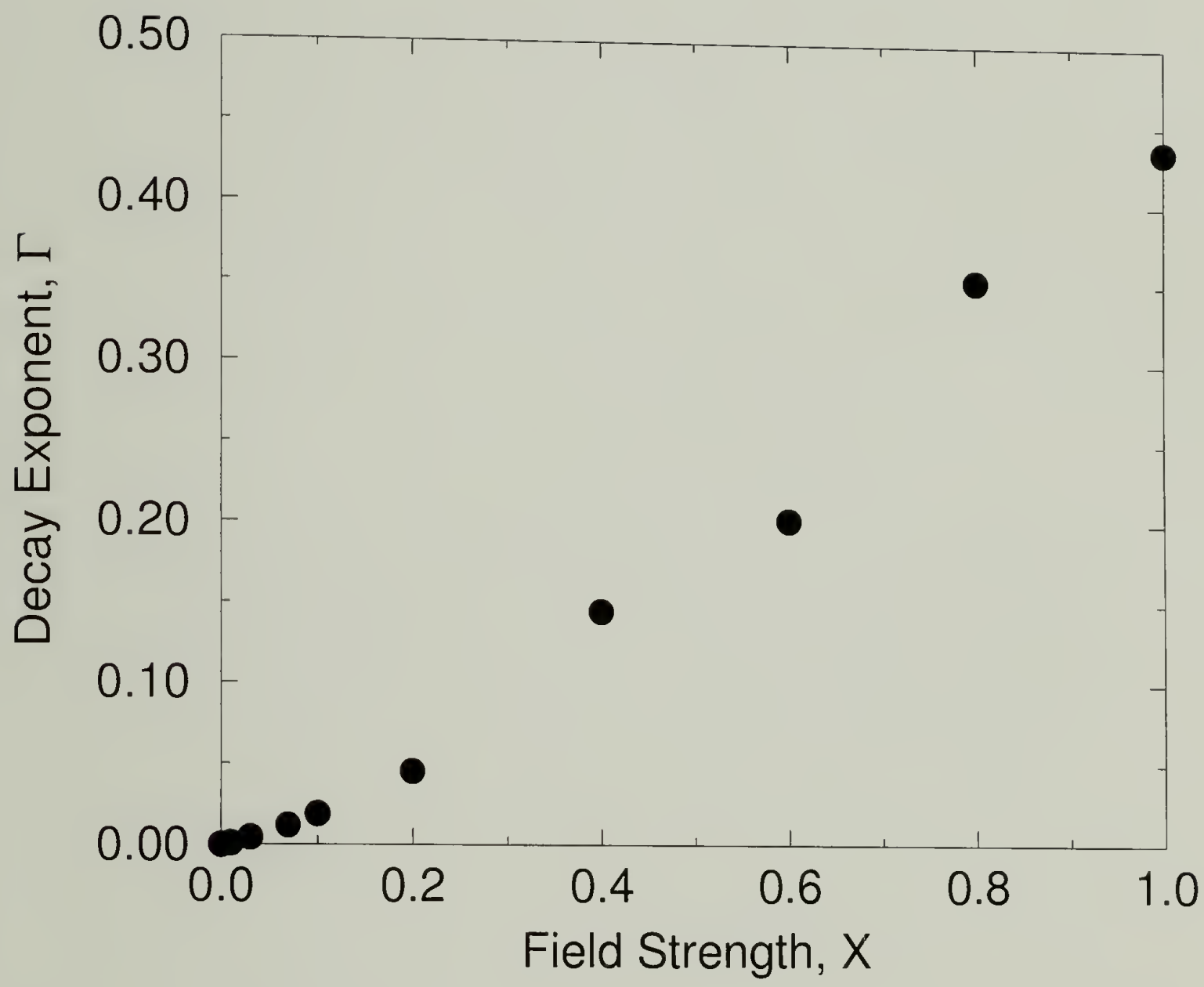

Figure 2.9 Dependence of decay rate Γ on X. Data correspond to the asymptotic slopes of the curves in Fig. 2.8.

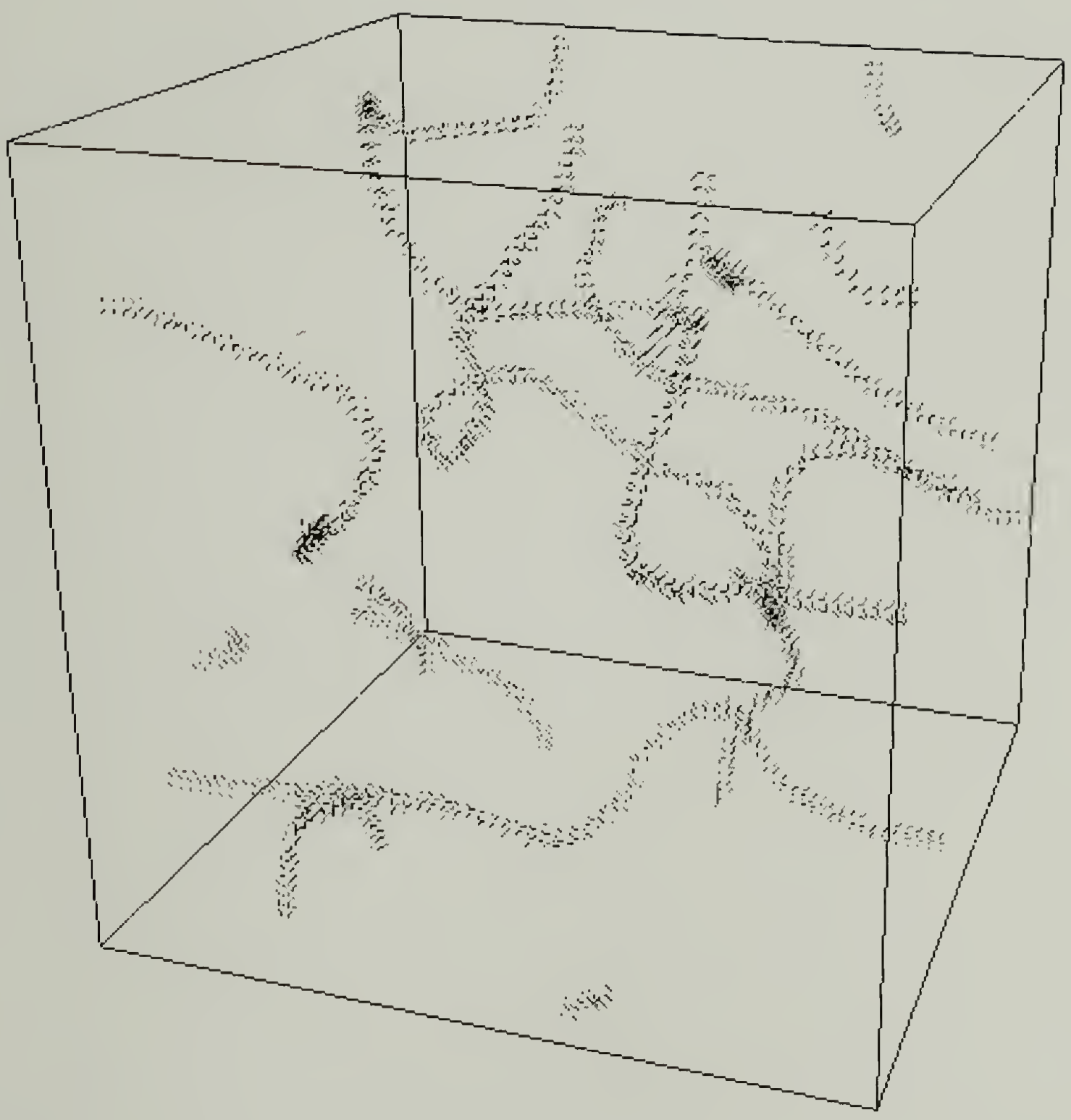

Figure 2.10 A typical configuration of disclinations in three dimensions.($N = 70, T = 0.04, K_{11} = K_{22} = K_{33} = 1, X = 0 = W$, at time step = 6349)

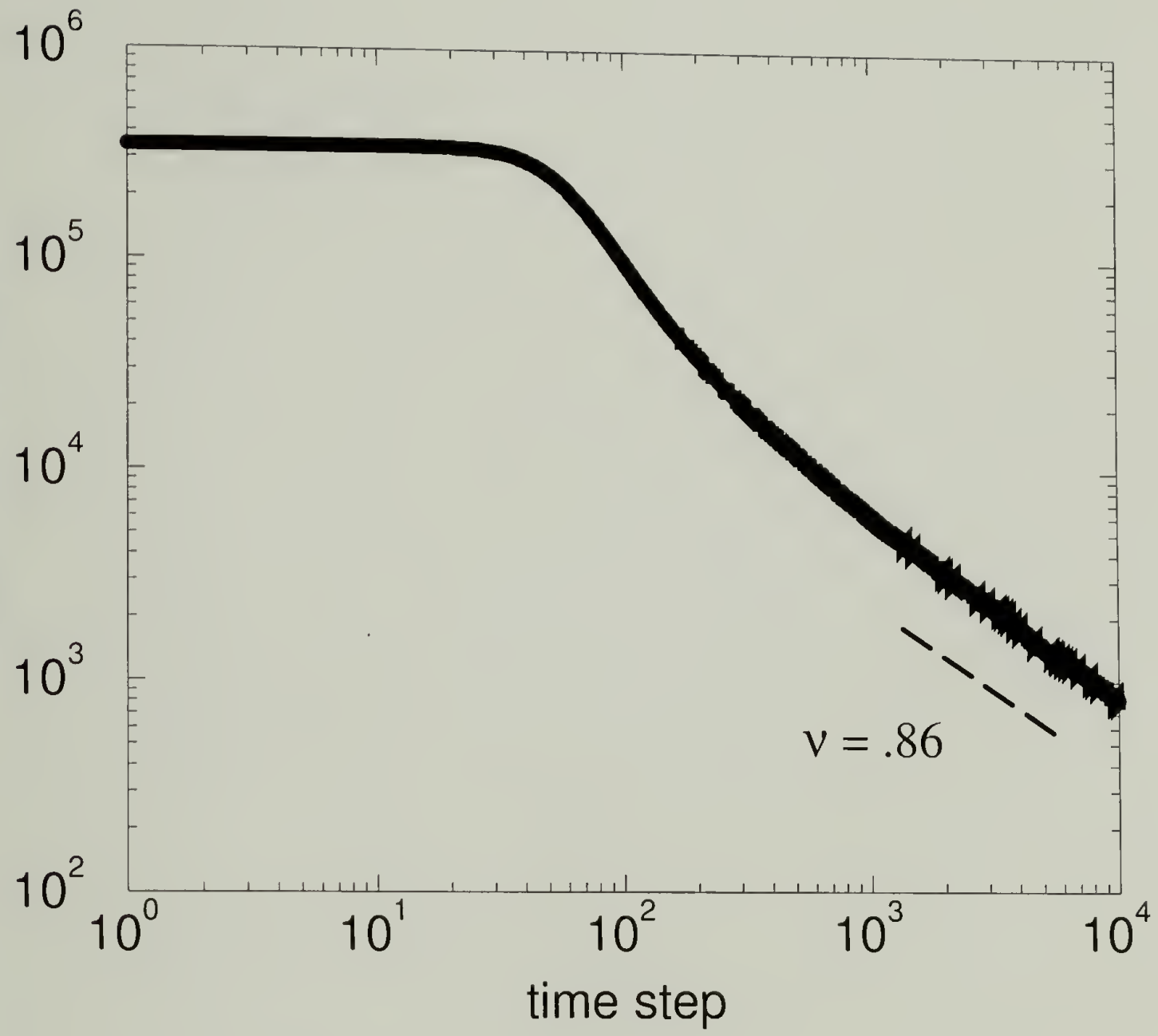

Figure 2.11 A typical evolution of disclinations in three dimensions. In the asymptotic regime, ν is 0.86. $(N = 70, T = 0.04, K_{11} = K_{22} = K_{33} = 1, X = 0 = W)$

CHAPTER 3

SIMULATION OF INVERSION WALL KINETICS

3.1 Introduction

Nematic liquid crystals, which often exhibit positive diamagnetic anisotropy ($\chi_a > 0$) but not spontaneous electric or magnetic polarization, react to the presence of an external electric or magnetic field by aligning either parallel or anti-parallel to the field. Furthermore, since the director orientation $\vec{n}$ is equivalent to $-\vec{n}$, there is a degeneracy between the parallel and anti-parallel states. If an external field is applied perpendicularly to an initial monodomain, the directors rotate and tend to orient along the direction of the external field. Inversion walls where the director rotates by a multiple of π across the walls develop between these domains of differing rotations.

Helfrich[55] first identified three types of alignment inversion walls. One is the twist wall, akin to the Bloch[56] wall in magnetic-spin systems where the wall is parallel with the field and the director orientation through the wall twists about an axis perpendicular to the wall. Another is the bend-splay wall, so called because the bend elastic deformation is predominant, akin to the Néel[57] wall in magnetic-spin systems where once again the wall is parallel with the field and the directors are in a plane traversing a U-shaped trajectory through the wall. The third is the splay-bend wall, which is perpendicular to the field and forms a cusp at the wall.

As mentioned previously, when a liquid crystal monodomain is subjected to an external magnetic field above the critical Freedericks field $H_c = \pi/d\sqrt{K/\chi_a}$ (where d is thickness, K is the elastic constant, and χ_a is the magnetic susceptibility) and normal to the orientation of the monodomain, regions of opposite rotation (*e.g.* clockwise vs. counterclockwise) will develop. Inversion walls form where these growing domains of similar rotations impinge on each other. For thin films, the walls appear as lines (Fig. 3.1). When one domain completely surrounds another, a loop will separate these two domains. The three-dimensional analogue is the bulk, where the walls appear as surfaces, as seen in Figure 3.2. Inversion walls are transient not only because they are more energetic compared to the monodomain, but also because they have simple ways to reduce that energy. Loops have been experimentally observed to divide, coalesce, and shrink, although under most conditions, the predominant method of loop size reduction is via shrinkage. [7] The exception is the applied external field being too strong, in which case the inversion wall breaks into equal but oppositely-signed disclinations and collapses quickly[7].

De Gennes[58] described the kinetics of a shrinking loop by a simple force balance analysis. The curvature of a loop drives the contraction of the loop. This radial force per unit length is $-\mathcal{T}/R$, where $\mathcal{T}$ is the line tension, defined as energy per unit length, and R is the radius. It is balanced by the friction force, which is friction coefficient, f, times the velocity of the wall, or dR/dt.

$$-\frac{\mathcal{T}}{R} = f\frac{dR}{dt} \tag{3.1}$$

DeGennes further showed that

$$f = \frac{\gamma_1}{K}\mathcal{T} \tag{3.2}$$

and

$$D_0 = K/\gamma_1 \tag{3.3}$$

where D_0 is the orientational diffusion coefficient, K is the elastic constant in the one constant approximation, and γ_1 is the drag coefficient. If we substitute Eq. (3.2) in Eq. (3.1), we get

$$-\frac{\mathcal{T}}{R} = \frac{\gamma_1 \mathcal{T}}{K}\frac{dR}{dt}. \tag{3.4}$$

After integrating the above expression we find that the loop shrinkage time scales as the square of the loop radius and inversely with the orientational diffusion coefficient.

$$t = \frac{R^2}{2D_0} \tag{3.5}$$

Brochard [59] derived a comprehensive and explicit set of derivations for wall dynamics in nematic liquid crystals. In the section on circular walls, she arrived at the following result:

$$\frac{\mathcal{T}}{R}s = s^2\gamma_1\frac{\mathcal{T}}{\chi_a H^2 \xi^2} \tag{3.6}$$

where s is the wall speed dR/dt and ξ is the magnetic coherence length

$$\xi = 1/H\sqrt{K/\chi_a} \tag{3.7}$$

as defined by deGennes[60] and H is the strength of the external magnetic field. Simplification of Eq. (3.6) yields:

$$s = \frac{K}{\gamma_1 R} \tag{3.8}$$

which is the same result as deGennes'. Verification of this important result is the goal of the simulations described in this chapter.

Looking at Eqs. (3.5) and (3.6), we see that both the total shrinkage time, t, and the wall speed, s, are not convenient measurements since they depend on the radius of the loop, which is constantly changing. Therefore, we rewrite them as:

$$\frac{dR^2}{dt} = \frac{2K}{\gamma_1} \tag{3.9}$$

so that the the non-varying parameters are isolated.

For measurements of dR^2/dt, in the two-dimensional simulations, we have chosen to monitor the shrinkage rate of the area enclosed by the loop, πR^2, henceforth referred to as loop area, and in three-dimensions we have chosen to monitor the shrinkage rate of the surface area of the ellipsoid, $4\pi R^2$, henceforth referred to as sphere area.

3.2 Simulation Method

The simulation was carried out using two and three dimensional lattices, with each lattice site containing a liquid crystalline director. The directors can rotate but not translate. In two dimensional lattices, the lattice is planar and only in-plane rotations are permitted. The orientation of the director is updated using the Metropolis algorithm in which, in each iteration, at every lattice site, a new director orientation with a maximum perturbation of $\pm$ 2 degrees is chosen, its new free energy is calculated, and the new orientation is accepted with the probability $\exp(-\Delta F/k_B T)$ where ΔF is the difference of the free energy, F, between the new

and the current orientation. In this simulation, F is the Frank free energy [62], given by

$$F = \frac{1}{2}\int dV\{k_{11}(\nabla\cdot\vec{n})^2 + k_{22}(\vec{n}\cdot\nabla\times\vec{n})^2 + k_{33}(\vec{n}\times\nabla\times\vec{n})^2\} - \frac{1}{2}\int dV(\vec{X}\cdot\vec{n})^2 \quad (3.10)$$

and discretized and expressed in two and three dimensions. V is the volume, k_{11}, k_{22}, and k_{33} are splay, twist, and bend elastic constants respectively, $\vec{n}$ is the director orientation, and $\vec{X}$ is the generalized external field given by

$$\vec{X} = \sqrt{\Delta\epsilon\ \epsilon_o}\ \vec{E} + \sqrt{\frac{\Delta\chi}{\mu_o}}\ \vec{B} \quad (3.11)$$

where $\vec{E}$ is the electric field, $\vec{B}$ is the magnetic field, $\Delta\epsilon$ and $\Delta\chi$ are the electric and magnetic susceptibilities, and ϵ_o and μ_o are the permittivity and permeability of vacuum. In two dimensions, the twist constant, or k_{22}, is not included because it represents out-of-plane distortions. Throughout the simulations we have used the reduced temperature T in units of the Boltzmann constant being unity.

Two programs were used to perform the simulations, one for the two-dimensional case and one for the three dimensional case. The two-dimensional lattice is used for studying loops composed of only splay-bend and bend-splay deformations (Fig. 3.3). The three-dimensional system is used for studying spherical inversion walls, which include all three types of inversion walls classified by Helfrich (Fig. 3.4). For the data presented here, the lattice size is 100x100 for the planar lattices, and 70x70x70 for the three-dimensional lattices. The initial loop or sphere diameter is approximately two-thirds of the dimension of the lattice.

Loop statistics are calculated by keeping track of which directors have rotated in the positive and negative directions. The directors inside the loop will all have the same rotational direction, so the space enclosed by the loop is a simple sum

over lattice sites with common rotational directions, and the size of the loop wall itself it a sum over all locations where the rotations reverse directions.

3.3 Results and Discussion

If we take a large 2-D lattice, uniformly aligned, and apply an external field perpendicular to the director orientation and in the plane of the lattice, many loops of random sizes may form in random locations. The term "loop soup" has been coined to describe this. A snapshot of such a system and its accompanying data is shown in Figs. 3.1 and 3.5. One can see that the contributions from the loops superimpose very well and that the number of loops in the system can be counted based on the sharp discontinuities following the termination of a loop. While it would not seem unreasonable to analyze data based on this randomly-generated loop soup, a cleaner simulation would be to study a system with only one well-defined, circular inversion wall.

We compare the scaling results from our Monte Carlo kinetics with the theoretical predictions. Figure 3.6 shows typical data for a two-dimensional lattice. Ignoring the initial time period during which the loop is forming, we see that the loop area shrinks linearly with time and the loop length (which is directly related to the radius as $2\pi r$) shrinks as the square root of time. The loop area and the loop length were determined independently. Similar agreement with theory is found in three dimensions. Figure 3.7 shows the data for a shrinking inversion wall sphere. Starting after about the 1000th time step, the sphere surface area (which is related to the square of the radius as $4\pi r^2$) decreases linearly with time and the sphere volume correctly scales as $t^{-3/2}$. The sphere surface area and the sphere volume were also calculated independently.

3.3.1 Effect of Field Strength

As described the introduction section, both deGennes and Brochard showed that the wall speed for inversion wall loops is independent of the field strength. To test this prediction, we simulated the loop shrinkage in both the 2-D program, which does not allow for K_{22}, or out-of-plane twist, and the 3-D program, which does. The lattice size was 100x100, the temperature was 0.05, and the elastic constants were unity. For brevity's sake, only the results for the 2-D program are shown here in Figure 3.8. Above $X = 0.4$ at the temperature of $T = 0.05$, the strength of the field causes the inversion wall to break into wall segments terminating in $+1/2$ and $-1/2$ defects, followed by rapid decay of the wall segments. This has been described in ref. [7]. Below $X = 0.2$, the field strength approaches the critical Freederickz point so we are limited to a narrow range. We see that the loop shrinkage rate is indeed independent of the field strength, contrary to intuition, though agreeing with theory. This can be explained because without the bias angle, the pressure per unit wall length from inside the loop is equal to the pressure from outside the loop, therefore the wall speed is dictated by the radius of curvature of the wall rather than the field strength.

3.3.2 Effect of Temperature

Both K and γ_1 in Eq. (3.9) are roughly inversely related to temperature, as shown by experimental evidence [17, 61]. Since they cancel out, one would expect at best a weak temperature dependence of loop shrinkage rate. This, however, is not borne out in the simulations.

In figure 3.9, we show the result for two-dimensional lattices, with the loop area shrinkage rate plotted versus inverse temperature. The elastic constants are

set to unity and the field constant, $X = 0.3$. Temperatures ranged from 0.01 to .08. Above $T = .08$, the size of the fluctuations hinders the accurate collection of loop statistics and below $T = 0.01$ the Metropolis acceptance ratio is too low for accuracy. Each data point represents the averaged value of 20 runs. The result shows a clear $1/T$ dependence for the loop area shrinkage rate. The difference between theory and simulation can be explained by the nature of Monte Carlo simulations. In evaluating the free energy expression $exp(-\delta F/kT)$, the elastic constant K is normalized by temperature, $1/kT$. However, there is no explicit term to account for the drag coefficient, therefore the temperature-dependent terms do not cancel out. In Monte Carlo simulations, quantitative comparison of kinetics as a function of temperature is difficult due to the inherent difficulty in mapping simulation time to real time.

3.3.3 Effect of Elastic Anisotropy

Brochard's theory likewise does not predict a dependence on elastic anisotropy. Nevertheless there are questions on the issues of loop ellipticity and splay-bend symmetry which we shall presently address.

Elastic anisotropy refers to the condition when the elastic constants, twist, splay, and bend, are not equal. In two dimensions we are only concerned with the splay and bend constants. When the constants are not equal, the different types of walls, either the bend-splay, splay-bend, or twist wall, will move at different speeds. The system will most quickly reduce the type of wall with the highest energy per unit length. In a 2-D loop without twist, the splay-bend wall will be oriented perpendicular to the field direction and the bend-splay wall will be oriented

parallel with the field direction. If $K_{11} > K_{33}$, the resultant loops will have their major axes aligned in the direction of the field and vice versa.

Since Brochard showed that the loop shrinkage speed depends on the value of the elastic constant but not the elastic anisotropy, we must define a set of constraints that will satisfy this requirement; that is to say, the sum of K_{11} and K_{33} must be constant while the ratio $\rho = K_{11}/K_{33}$ changes. We have chosen $K_{11} = 1$ and $K_{33} = 1$ as our starting point, so for any given elastic ratio ρ,

$K_{11} = 2\rho/(1+\rho)$

$K_{33} = 2/(1+\rho)$.

Figure 3.10 shows that indeed the loop shrinkage rate is independent of ρ as long as $K_{11} + K_{33} = const.$ We also found (not shown here) that the loop area shrinkage rate is independent of the initial shape of the loop, whether circular or elliptical.

The ellipticity of the loop and the thickness of the wall are direct consequences of the elastic constants, and hence can be used as a method to compare experimental observations with theoretically derived values. Building on Brochard's [59] work, Leger [9] showed that the thicknesses of the splay-bend, bend-splay, and twist walls are proportional to $\sqrt{K_{11}}$, $\sqrt{K_{33}}$, and $\sqrt{K_{22}}$, respectively. Furthermore, it was shown that the ellipticity or aspect ratio of the loop, a/b, is proportional to $\sqrt{K_{11}/K_{22}}$ for a splay-bend and twist-bend loop, with similar results for other loop geometries. Ding and Thomas [6] report quantitative values of elastic anisotropy from direct measurements of the director field.

We measured the ellipticity of the loops for a range of elastic anisotropies. We defined the elastic ratio, ρ, as K_{11}/K_{33}. For any given initial shape of the loop, the loop evolved toward some asymptotic ellipticity which depends on the elastic ratio. This asymptotic shape is realized just before the loop disappears. We

found, as shown in Figure 3.11, that the ellipticity does indeed increase at the rate proportional to $\sqrt{K_{11}/K_{33}}$.

3.4 Conclusion

We have undertaken to verify the equation describing the dynamics of inversion wall loop and sphere shrinkage as derived by deGennes and Brochard. Our simulations show that R^2 decreases linearly with time, and the rate of shrinkage is dependent solely on the orientational diffusion coefficient, which encapsulates the effect of the elastic constant and temperature. Also significant is the independence of the shrinkage rate with the field strength and elastic anisotropy.

The simulation was also shown to accurately yield the correct asymptotic ellipticity of the loops when elastic anisotropy is varied.

We have also shown the first known computer simulation images of inversion walls in three dimensions and verified that in three dimensions the scaling relationship by deGennes and Brochard still holds true.

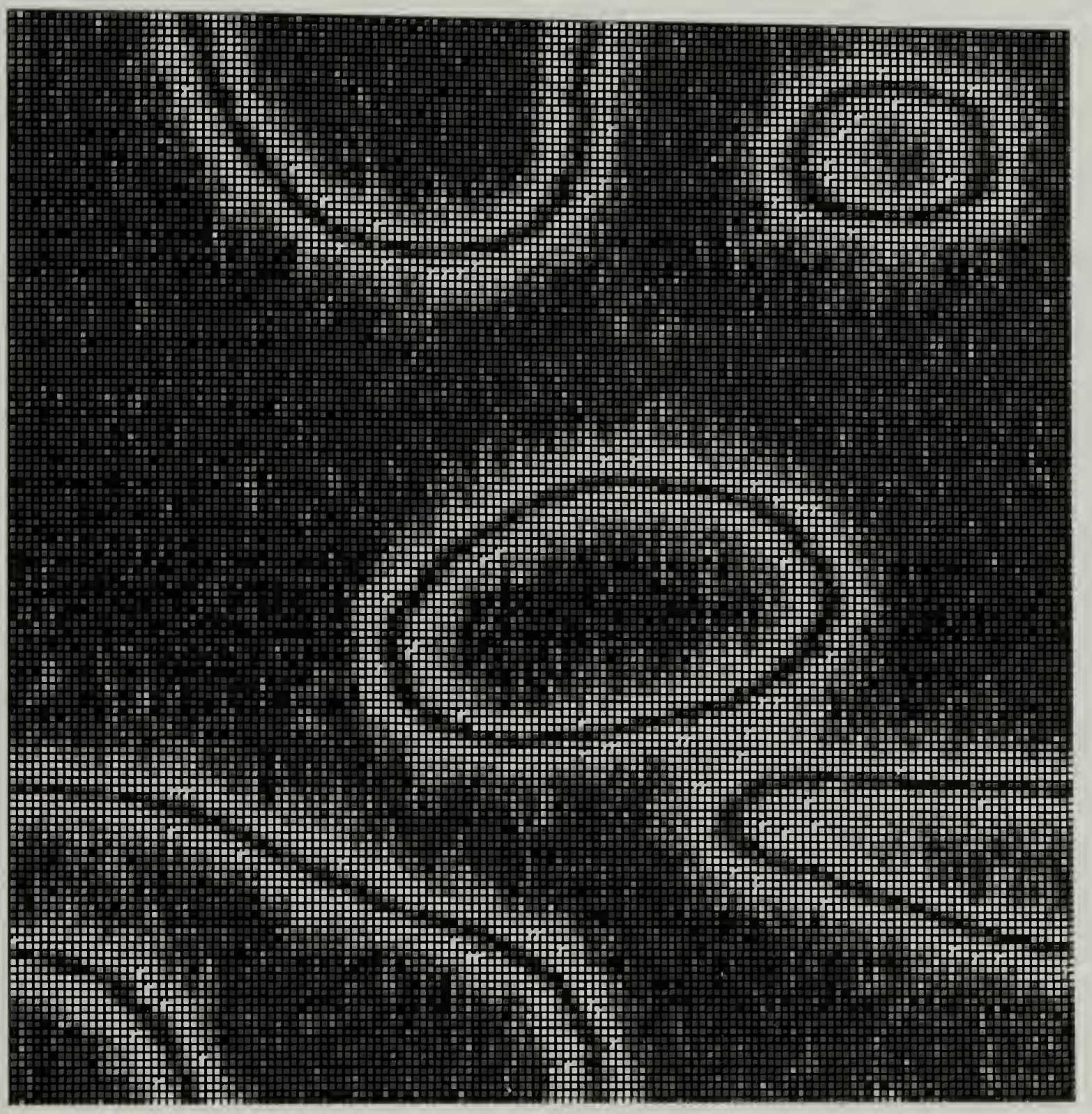

Figure 3.1 Randomly created inversion walls in two dimensions. Lattice size is 150^2. Temperature is .05 and field strength is .3.

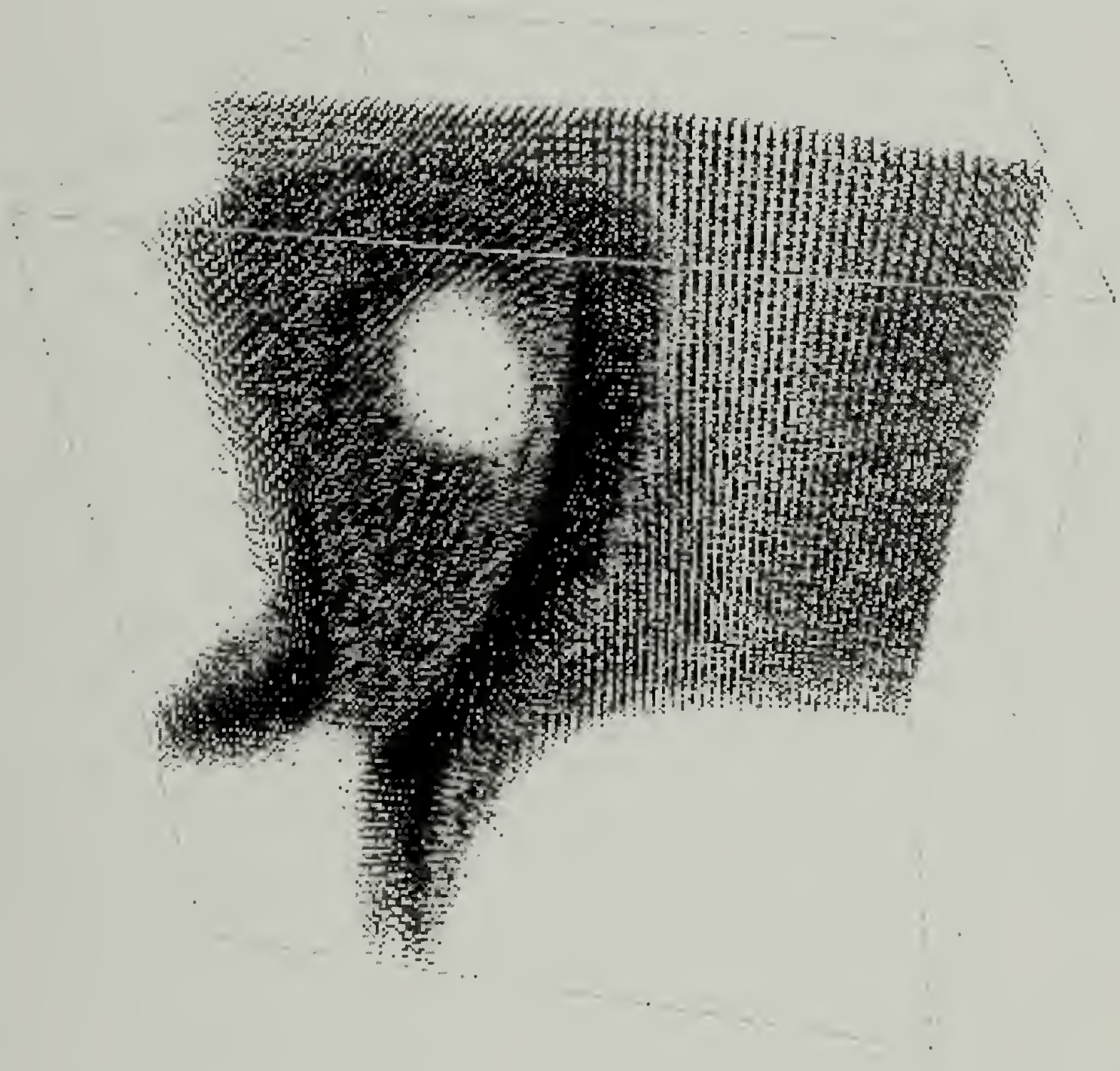

Figure 3.2 Randomly created inversion walls in three dimensions. Lattice size is 60^3, temperature is .01, field strength is .15.

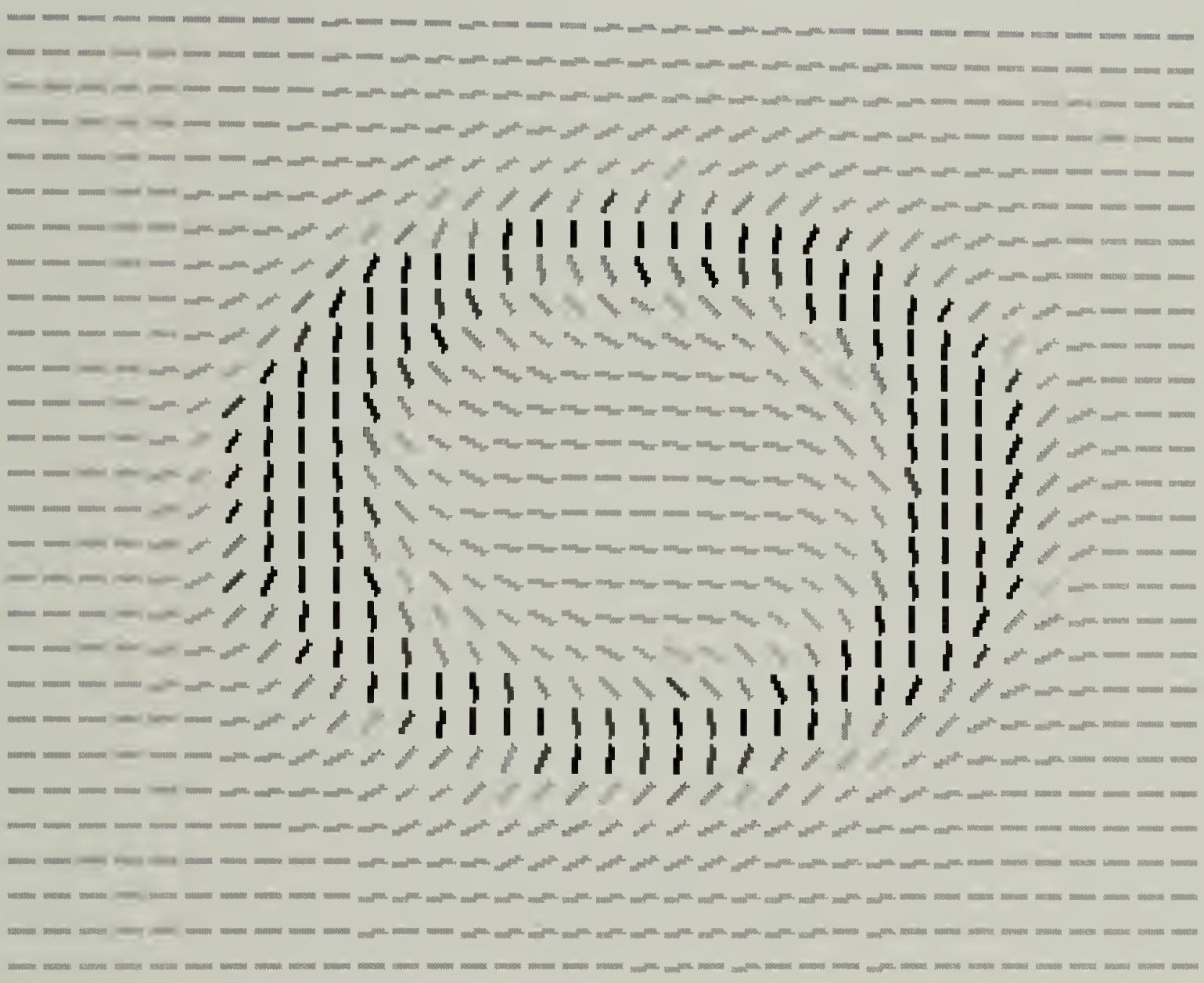

Figure 3.3 A typical 2D inversion wall loop. Lattice sites with high elastic energy are drawn darker.

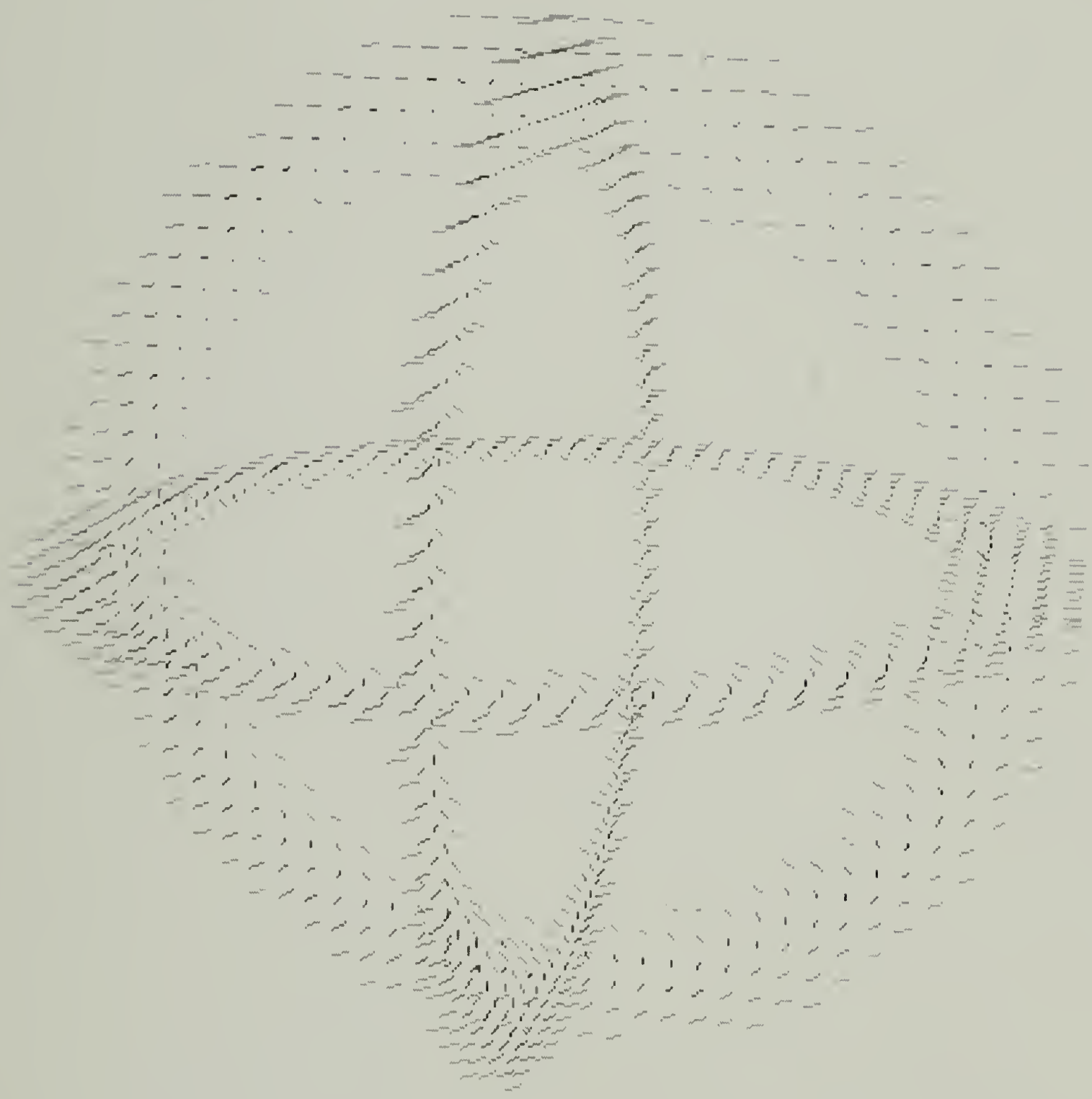

Figure 3.4 X, Y, and Z-plane slices through the center of an inversion wall sphere. Lattice size is 70^3, temperature is .01, and field strength is .15. Twist, splay, and bend deformations are visible in various portions of this view.

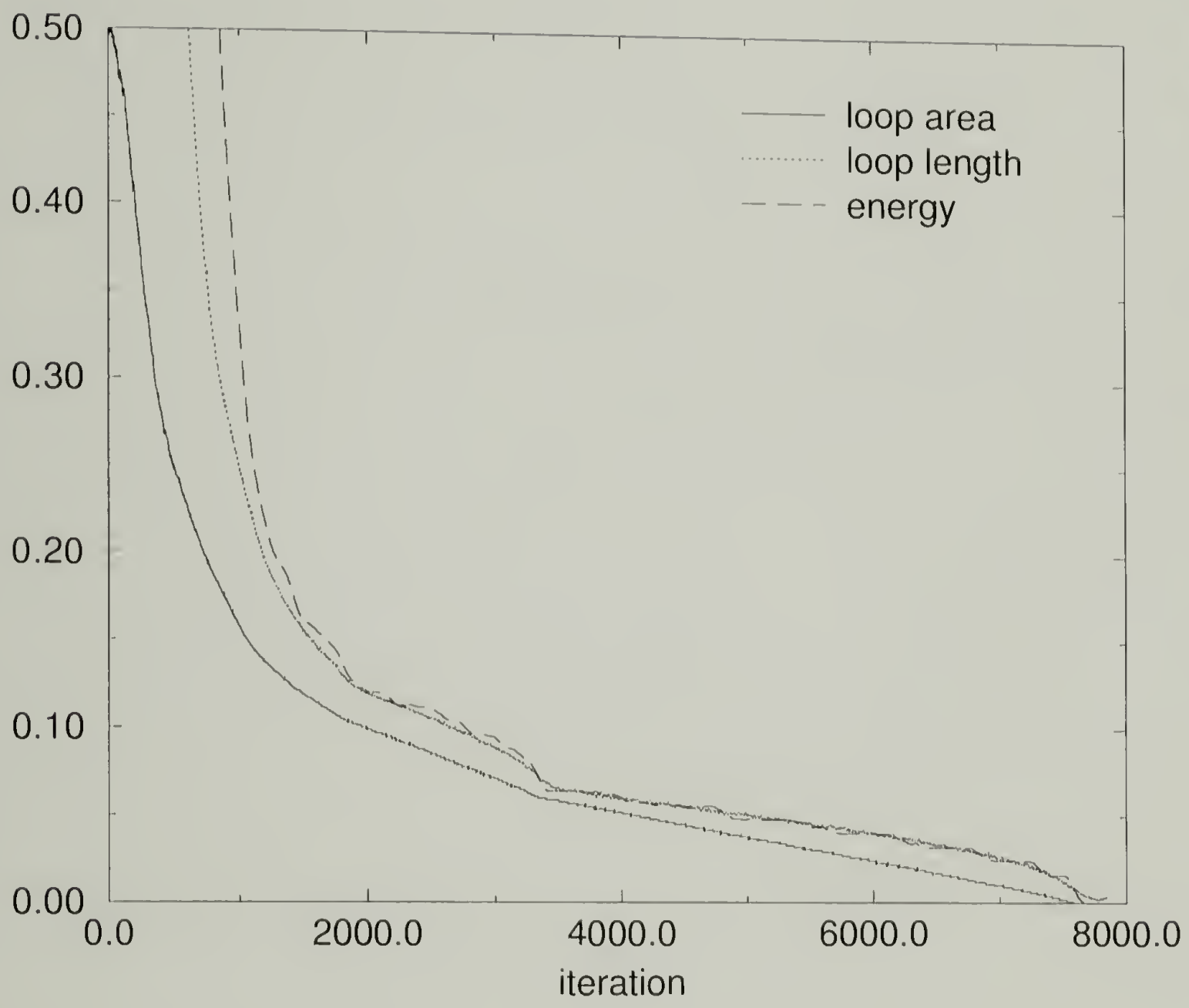

Figure 3.5 Data for randomly created inversion walls in two dimensions. Parameters are the same as for Figure 3.1. All units have been rescaled in order to compare the relative changes over simulation time.

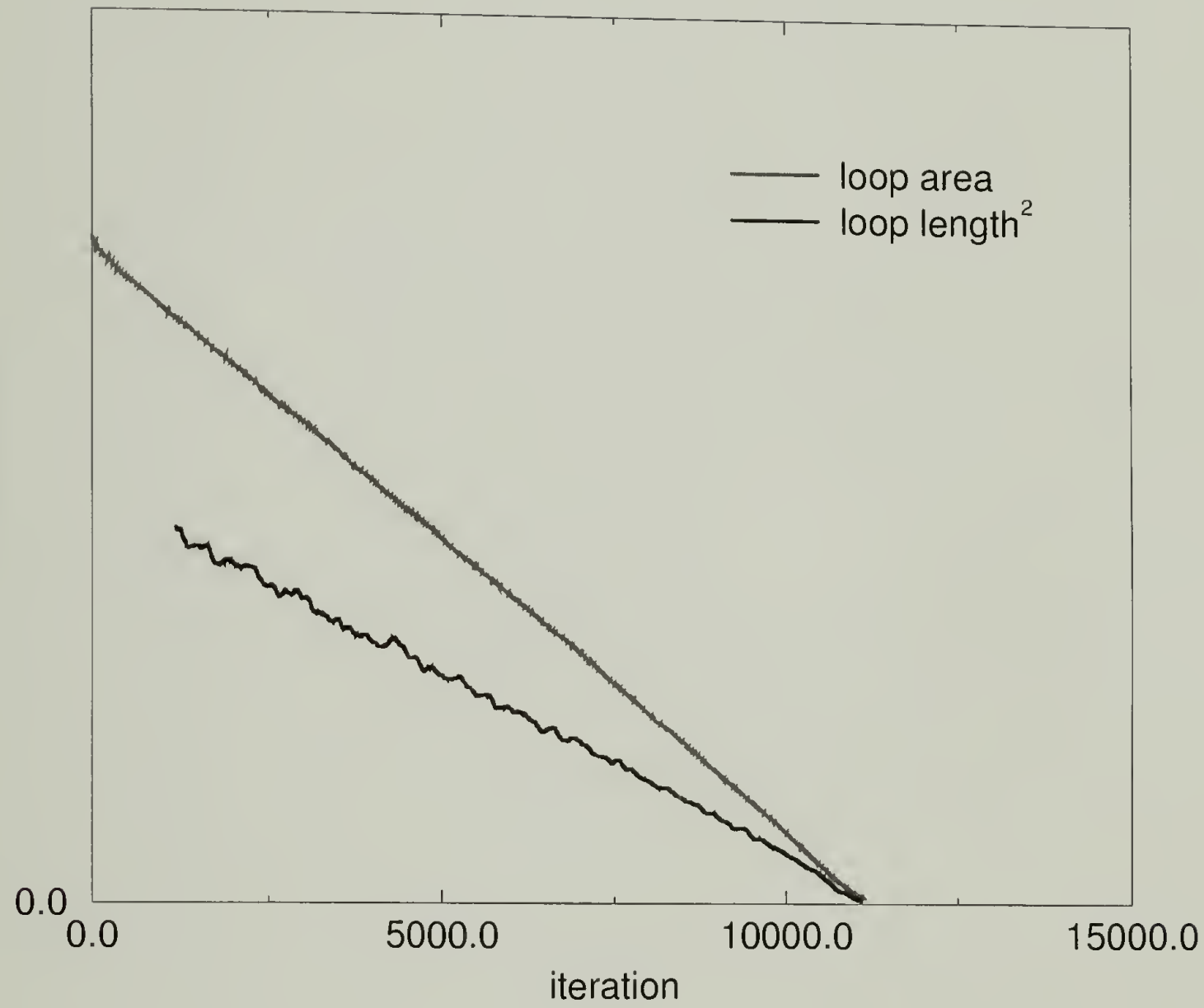

Figure 3.6 Plot of loop area and square of loop length for a typical 2D loop shrinkage. Units have been rescaled. The $R^2 \sim t$ relationship is apparent.

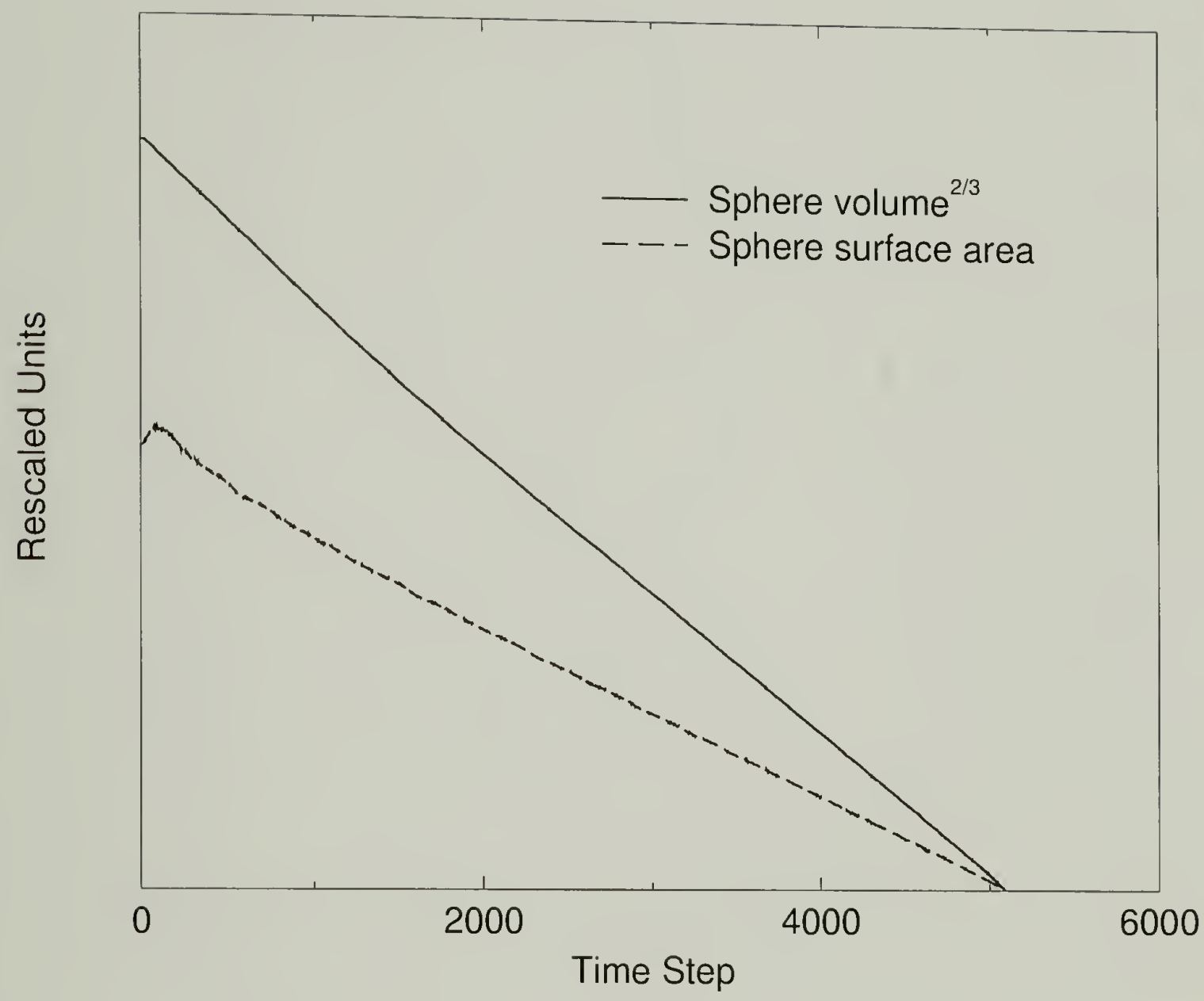

Figure 3.7 Typical sphere volume and sphere surface area data from a 3D sphere shrinkage simulation. This particular data was taken from a simulation with lattice size of 70^3, temperature of .01, and field strength of .2. Data is plotted to show that R^2 is linear with time in three dimensions as well.

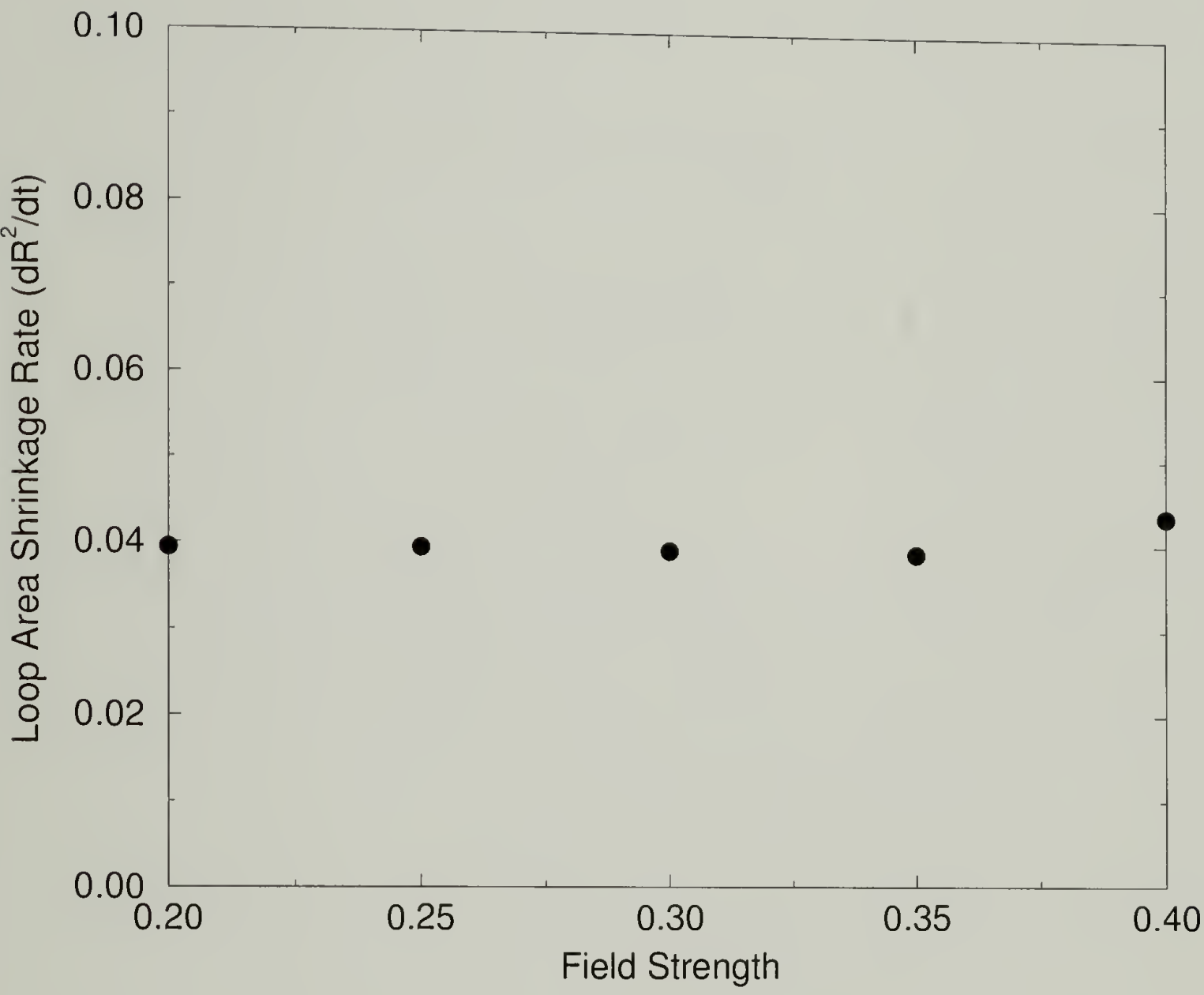

Figure 3.8 Plot taken from runs with lattice size of 100^2 and $T = .05$ shows that shrinkage rate is not dependant on field strength.

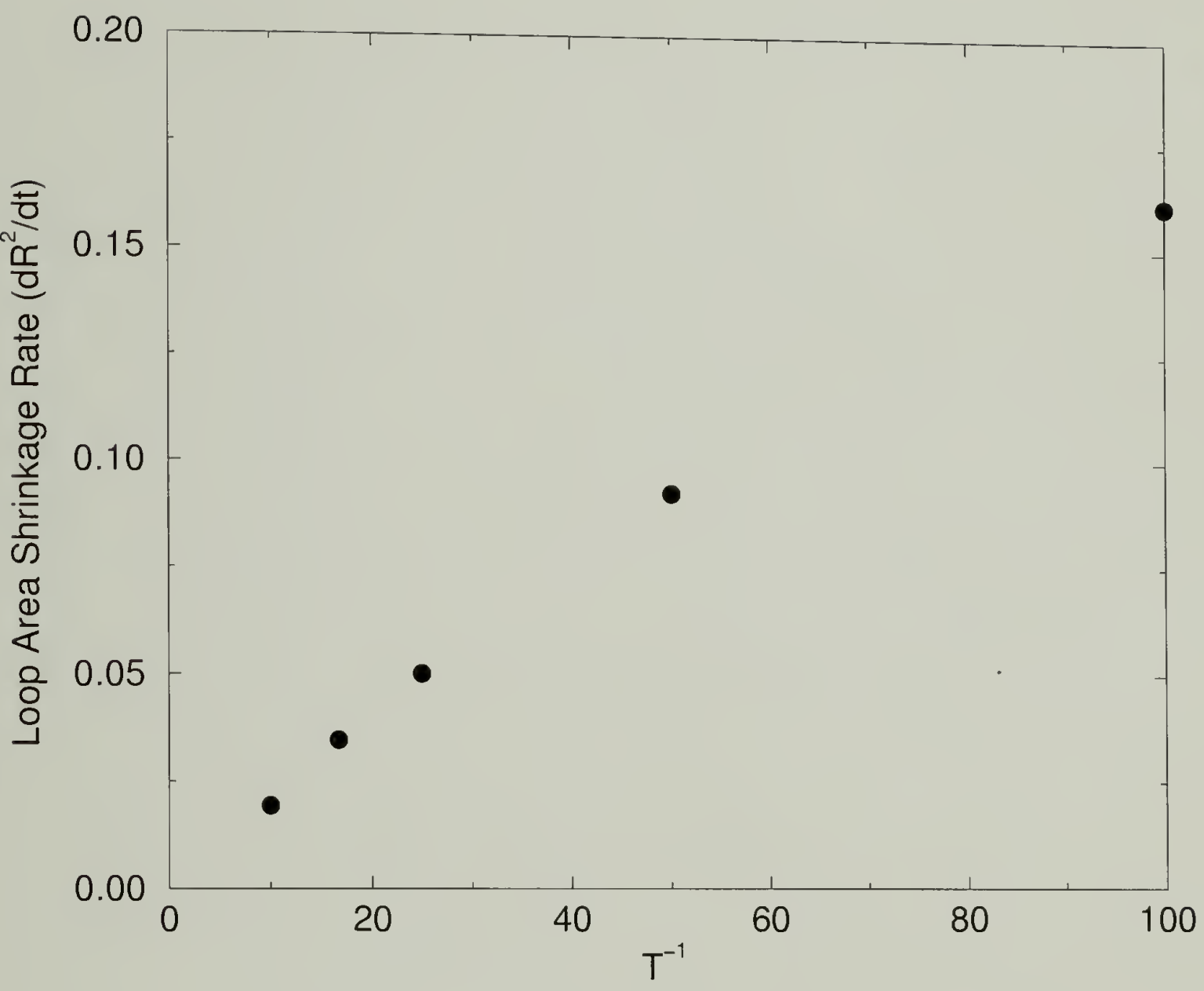

Figure 3.9 The loop area shrinkage rate shows a T^{-1} dependence for which the explanation can be found in the text. Lattice size is 100^2 and field strength is .3.

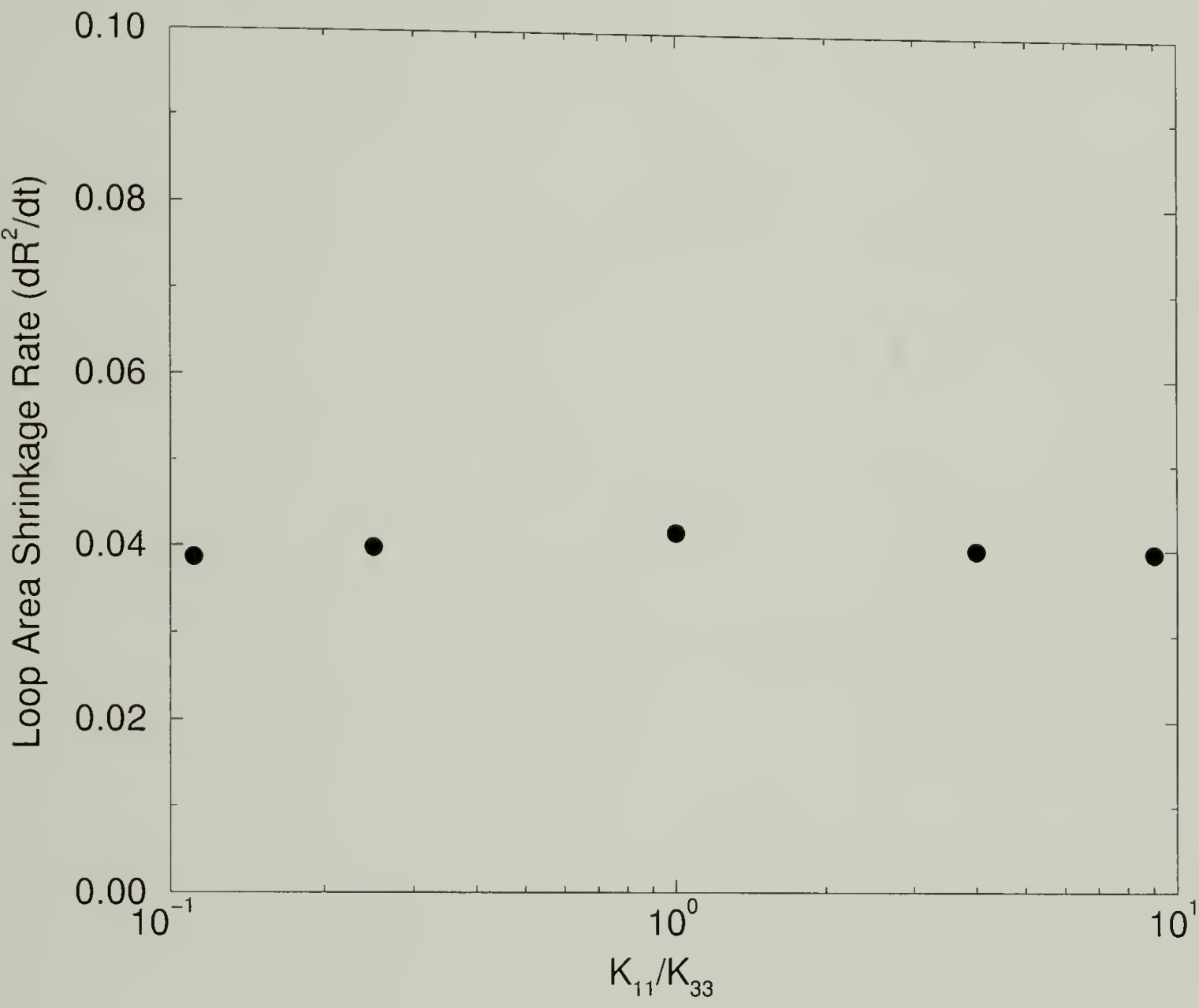

Figure 3.10 Shrinkage rate is not dependent on the elastic anisotropy, K_{11}/K_{33}. The ratio is plotted on a log scale with the equal elastic constant point in the center. Temperature is .05 and field strength is .4.

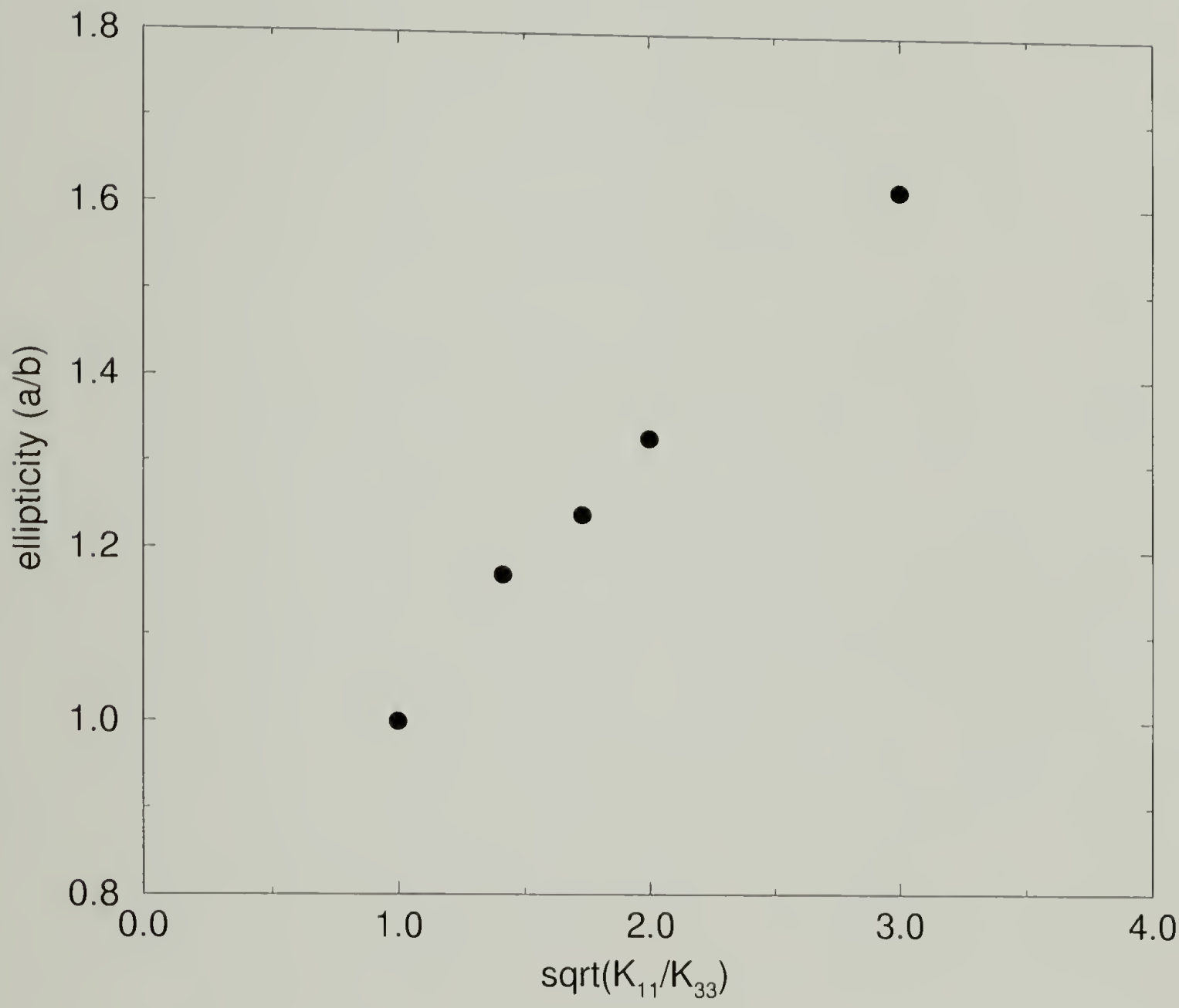

Figure 3.11 The aspect ratio of the loops scales as $(K_{11}/K_{33})^{1/2}$. Simulation performed at temperature of .001 and field strength of .2 in order to make the loops well-defined and easy to measure.

CHAPTER 4

LANGEVIN DYNAMICS SIMULATIONS OF EARLY-STAGE POLYMER NUCLEATION AND CRYSTALLIZATION

4.1 Introduction

It is known that in dilute solutions certain polymers fold and crystallize in the form of thin single crystals and in the melt certain polymers form spherulites. Several books [63, 64], recent review articles [65, 66], and discussions [67–69] cover this subject extensively. Many proposals to explain the mechanism of polymer crystallization have been made [63–78, 80]. The experiments and models generally focus on one of three basic regimes in polymer crystallization. If impurities or seed nuclei are not present, it is necessary for homogeneous nucleation to occur before a crystal can develop. Once a nucleus comes into existence, additional layers of polymer chains can then adsorb and crystallize; this regime is usually termed secondary nucleation and growth. In dense polymer systems where spherulitic formation is commonplace, a third regime called secondary crystallization may be present, where macroscopically the spherulites are volume-filling, but crystallization continues microscopically in the amorphous regions between lamellae.

Nucleation can occur when the polymer solution or melt is supercooled. For homogeneous nucleation, the number of nuclei is assumed to be first order in time.

In the thermodynamic view, the decrease in bulk free energy upon the formation of a nucleus is offset by the rise in free energy from creating surfaces. The model holds that due to density and orientation fluctuations many attempts at forming a thermodynamically stable nucleus are made and the number of stable nuclei formed increases with supercooling. At even greater supercooling, fluctuations diminish and therefore the rate of nucleation diminishes [63].

Recently, kinetic theories of crystal growth have come to dominate the field. Based on the observation that the lateral growth rate of dilute polymer crystals is independent of the size of the crystal, the kinetic theories follow the idea of separating growth into two basic components – the nucleation of a chain segment onto a clean surface and the adsorption and desorption of additional chain segments onto a populated surface. In the classical model, Hoffman and Lauritzen [71] envisioned this process taking place with complete chain stems, each the thickness of the lamella. They believed that the rate-limiting factor was the free energy barrier associated with the creation of a step on a clean surface. Sadler proposed an alternative model in which the consideration of surface roughness and molecular 'pinning', both entropic barriers, gives a result more in agreement with experiment [72–74]. It is of continuing interest to identify the experimental conditions where these models are applicable.

There are also finer-grained models which seek to more accurately describe the physical process. Models such as that by Point [76] consider the attachment and detachment of individual segments and allow for folds anywhere on the growth front, not just at the fold surfaces of the crystal. The accuracy of these models is often determined by comparison with experimental measurements of growth rates and lamella thicknesses. However, the ability to answer the question of whether these models are physical has been hampered by lack of direct experimental observations

of the molecular motions involved with nucleation and growth. It has become apparent that different assumptions can often lead to the same results and the body of experimental results is not able to prove or disprove these theories. Recently, there has been increasing interest in a computational solution to the most fundamental question of how polymers crystallize. Some of the models are summarized below.

To simulate secondary nucleation on a growth front, Yamamoto [80] proposed a model in which a polymer chain is freely-jointed and strongly adsorbed to a surface, confining it to two-dimensional motion. The surface consists of parallel potential valleys, which emulate the potentials of a crystalline surface. The chain aligns preferentially along the valleys, but must cross over potential hills at the folds. This model was able to reproduce phenomena such as lamellar thickening and the coalescence of small crystallites into larger ones. The author concluded that the van der Waals attraction between the chain and the surface is the driving force for crystallization and lamellar thickening.

More realistic models can be attained by using fewer assumptions. Computer simulations of chain-folding of a free-floating polyethylene molecule in three dimensions have been reported by Kavassalis and Sundararajan [77]. Starting with an all-*trans* conformation, the chain-collapse and subsequent lamella formation resulted in a lamellar dimension that was below experimental values. This led to the realization that the torsional barrier was key to controlling lamellar dimensions and new results were later published [78]. Their breakdown of the energies in the system, namely torsion, bond angle, and van der Waals energies, show that at chain lengths greater than 150 methylene units, the increasingly strong van der Waals interactions outweigh the energy penalty from the *gauche* torsional conformation, making the folded configuration energetically preferable to the extended-chain configuration. This is in agreement with some experimental results [79].

The observation that lamellar thickening occurs and is not reversible [63] has led to the popular view that polymer crystallization is largely a kinetically-controlled process [66]. It is also observed that the thickness of the lamella is independent of molecular weight for chains of more than several hundred monomers. What is not presently known is whether a lamella thickens by simultaneous readjustment of all stems in the crystal, or whether a chain fold is pulled completely through the crystal, thus doubling the length of the stems. This largely unknown process is especially suitable to investigation via computer simulations.

In an attempt to address the above issues, we have performed Langevin dynamics simulations. In this chapter we first present results on the primary nucleation of single chains at various degrees of undercooling and report the evolution of the order parameter during the process. We closely examine the interplay of individual chain segments leading up to the formation of an identifiable nucleus. We then discuss secondary nucleation and identify rate-limiting factors in lamellar growth. We also investigate the effects of chain length to growth front thickness mismatch. Finally, we present results on collective behavior of several chains crystallizing simultaneously. We provide clear evidence of quantization effect in lamellar thickening and compare with known experimental results.

4.2 Simulation Method

The simulation model attempts to incorporate just enough detail to observe chain-folding without impeding the efficiency of the simulation. As a result, the united atom model for polyethylene is chosen for a polymer chain, in which each methylene unit is treated as a bead in a bead-spring model. Typical chain lengths in our simulations range from 100 to 1000 united atoms. The force field parameters

are modeled after the paper by Paul *et al.* [81], which are in close agreement with experimental measurements on the polyethylene melt. One modification is that in our model, the terminal methyl group has the same force field parameters as the methylene units.

The total potential energy consists of the potential energy of each bond arising from bond stretch U_r, bond angle U_θ, and bond torsion U_ϕ, and non-bonded bead-bead interaction which is taken to be the Lennard-Jones interaction U_{L-J}. The potential energy associated with bond stretch is taken to be

$$U_r = k(r - r_0)^2$$

where r is the bond length and r_0 is the equilibrium bond length. The spring constant k is taken to be 350 $kcal/mol \cdot \mathring{A}^2$ and $r_0 = 1.53\mathring{A}$. The potential energies associated with bond angle θ and torsion angle ϕ are assumed to be of the form

$$U_\theta = k(\theta - \theta_0)^2$$

and

$$U_\phi = k_1(1 - \cos\phi) + k_2(1 - \cos 2\phi) + k_3(1 - \cos 3\phi)$$

where $\theta_0 = 109°$, $k_\theta = 60$ $kcal/mol$, $k_1 = .8$ $kcal/mol$, $k_2 = -.43$ $kcal/mol$, and $k_3 = 1.62$ $kcal/mol$. The Lennard-Jones potential U_{L-J} is

$$U_{L-J} = \epsilon[(\sigma/r)^{12} - 2(\sigma/r)^6]$$

where the interaction strength ϵ and the equilibrium distance σ are taken to be .112 kcal/mol and 4.5 $\AA$, respectively. The Lennard-Jones interaction contains a coefficient of 2 for the attractive part so that the minimum of this potential occurs at $r = \sigma$.

For the actual computation, reduced units are used throughout and all data presented here are expressed in terms of the reduced units. The units have been renormalized to a united-atom mass m of 1, an equilibrium bond length r_0 of 1, and a Lennard-Jones ϵ of 1. It follows that the reduced temperature, T^*, is equal to $k_B T/\epsilon$, the reduced energy is E/ϵ and the reduced time is $t\sqrt{\epsilon/m\sigma^2}$.

The magnitude of the force field parameters show that the bond length and the bond angle are basically rigid and it is the torsional angle that changes the most during the simulation. We have found that the exact choices of bond length stiffness and bond angle stiffness are unimportant as long as they are high relative to the torsional angle parameters.

The equations of motion are integrated according to the methodology of Langevin dynamics[12, 83]. In Langevin dynamics, the motion of the particles is described by the Langevin equation (Eq. (4.1)) which consists of inertial terms, force field, frictional drag, and noise, respectively [12, 83].

$$\ddot{r}_i = -\nabla U_i - \Gamma \dot{r}_i - W_i(t) \tag{4.1}$$

The Langevin dynamics method simulates the effect of individual solvent molecules through the noise W, which is assumed to be Gaussian. The friction coefficient Γ is related to the autocorrelation function of W through the fluctuation-dissipation theorem,

$$\langle W_i(t) \cdot W_j(t') \rangle = \delta_{ij}\delta(t - t')6k_BT\Gamma. \tag{4.2}$$

Furthermore, we have set Γ to be 1, between the over-damped regime and the purely deterministic regime. We have used the velocity Verlet finite-differencing scheme[12, 84] for integration. This scheme, at larger time steps, is comparable in accuracy to the Gear predictor-corrector algorithms[85], but requires less memory and is simpler in implementation. In the velocity Verlet algorithm, the velocities of the particles are calculated at every half time step, leading to greater accuracy. The average time step used in the data presented here is about 0.01. An adaptive method is used in which the step size is adjusted to maintain a low integration error. Since in Langevin dynamics the effect of the solvent is implicit, we can only estimate the relationship between simulation time and real time. Due to the coarse-grained nature of the united-atom model, the time unit is expected to be longer than that of an atomistic model, on the order of monomeric relation time rather than atomic relaxation time. Based on the example of liquid argon [11], the relaxation time for a typical solvent molecule is of the order of 10^{-12}s. We therefore expect the relaxation time of the united atom to be also of the order of 10^{-12}s. Since in each iteration of a Langevin dynamics simulation the noise is uncorrelated and the time step is about 0.01, one time unit in our simulation is about 10^{-10}s. The precise relationship between the time unit used in the Langevin dynamics simulations performed here and the actual time is not yet established. Throughout the simulations, data are collected at periodic intervals. These include the radii of gyration of both labelled chains and aggregates, kinetic and potential energies, and the local and global order parameters.

In order to monitor how stems are oriented with respect to each other in a growing lamella, we identify an orientational vector at each bead i, $(\vec{r}_{i+1} - \vec{r}_{i-1})$, connecting the positions of neighbors of i. For a stem with only *trans* conformations, the linearity of the stem is better captured by this choice of orientational vector than the bond vectors $(\vec{r}_{i+1} - \vec{r}_i)$. We then construct an order parameter S by calculating the angles Φ between the various orientation vectors and performing the average over all possible pairs of orientation vectors,

$$S = \frac{< 3\cos^2(\Phi) - 1 >}{2}. \tag{4.3}$$

We have monitored the value of S for the whole chain (and the aggregate for the case of many chains) and we call this the global order parameter. In addition we have also computed the local order parameter where the volume element extends only over 2σ but averaged over throughout the chains.

4.3 Single-Chain Primary Nucleation

Before performing simulations on crystallization at various degrees of undercooling, we first determine the melting temperature of the polymer chains. We create an initial random configuration of an isolated chain of length 500 and equilibrate it at the reduced temperature of $T^* = 15$. We then quench to $T^* = 10$ and hold the temperature for several thousand time units until we observe a single stable folded structure to have formed. Starting from this temperature, we commence the monitoring of potential energies and order parameters. We perform several runs at heating rates ranging from .0001 to .002 T^*/time unit. Discontinuities are observed in the slopes of the total potential energy and the global order parameter at the

onset and ending of melting. The actual melting point is taken to be the extrapolation of the onset of melting to zero rate of temperature change. This temperature is estimated to be $11.0 \pm .2$ based on the average over four chains at each heating rate.

We proceed to study the case of primary nucleation, in which a chain folds into a crystal in the absence of impurities or seed nuclei. Figure 4.1 shows a typical sequence of images depicting this event and the values of time are indicated in the frames. A chain of 700 units is equilibrated above the melting point ($T^* \simeq 11$) and quenched to $T^* = 9$. The time steps shown in the sequence are selected from representative configurations observed during the course of the crystallization. Starting from the initial configuration shown in frame (a), the time evolution progresses to frame (f). A bundle of relatively straight stems can be seen in the early stages which attracts more stems to form a stable crystal. If the quench depth is shallower then thermal fluctuations can cause these bundles to form and fall apart; not all bundles reach the critical size for stable growth.

The global and local order parameters for this simulation are shown in Figure 4.2. The development of local order parameter proceeds quickly, reaching a plateau, then only increasing slowly over time. The global order parameter develops in a similar but slower fashion, delayed by a time interval.

We now proceed to study the role of undercooling on the lamellar thickness. We generate random configurations of four chains of 500 beads each and place them far apart in an infinitely large volume so that they do not interact with each other. We then equilibrate the system at $T^* = 15$, above the melting point. The equilibrated configuration is stored and used as the starting point for temperature quenches to various degrees of undercooling. After the temperature quench and after lamellar thicknesses have stabilized, we record the average radius of gyration of the lamellae

at the various undercoolings. The lamellar thickness for the chains crystallized at lower temperatures ($T^* < 10$) remain essentially unchanged while the chains at higher temperatures ($T^* \geq 10$) experienced thickening.

The thickness of the single crystal formed during isothermal quench is expected to be proportional to the inverse of the degree of undercooling[66]. The $1/\Delta T^*$ relationship has also been verified experimentally by Organ and Keller[86]. Figure 4.3 is a plot of the radius of gyration averaged over four isolated chains at each undercooling against $1/\Delta T^*$, where $\Delta T^* = 11.0 - T^*$. The plot is approximately linear, indicating agreement with expected results.

4.4 Addition of Chain to Growth Front

Secondary nucleation and growth have received intense scrutiny, as evident from the volume of research and review articles [65, 66] cited in the introduction of this chapter. It is the regime that is most easily observed experimentally with optical and scattering techniques. To simulate this regime, we isolate the model to where the growth is taking place, namely the growth front at the edges of lamellae. The growth front is modeled by a two-layer-thick wall consisting of 20 extended-chains of 50 beads each. All beads on the growth front are fixed in space so that a stable growth front can be simulated with a minimum of beads. While this growth front does not have folds and irregularities that actual lamellae would have, it is well-defined and suited for this study.

In addition to visualizing the crystallization process, we also seek to determine the effect of varying the chain length relative to the lamellar thickness. Since the inclusion of chain ends inside the crystal is energetically unfavorable (akin to the inclusion of impurities), we can choose a case where the chain length is not an

integer multiple of the lamellar thickness and see how the chain is accommodated on the growth front.

For the first case, we have chosen a chain of length 100 at $T^* = 8$, which should fold once on a growth front of length 50. Figure 4.4 shows the sequence of one such event and the values of time are indicated in the frames. The chain at first appears to be loosely captured by the growth front but the bulk of the chain soon aligns with the orientation of the substrate and adopts a once-folded configuration. The last frame (f) shows the final configuration where the chain has a single hairpin fold and is in perfect registration with the substrate. Frame (e) is particularly interesting because the kink near the bottom shows one mechanism by which the chain stem migrates from one site on the substrate to another.

For the second case, we have chosen a chain of length 125, which is not an integer multiple of 50. As seen in Figure 4.5, the chain explores many possible energy-minimizing conformations. Frame (c) shows two hairpin folds, similar to the previous case except with half a stem folded on the crystal. Because the stability of the crystallized chain is dependent on the competition between the energy gained from attached stems versus the energy lost from creating the hairpin turns, the energy of the half-stem is not enough to offset the energy of the additional fold. This causes the chain to explore other conformations, such as in frame (d) where the chain ends dangle off the substrate and frames (e) and (f) where the chain incurs an energy penalty in losing its registration with the surface.

The stability of the chains can also be observed in the time plots of the local order parameter (Figure 4.6). For the chain of $L = 100$, the local order parameter reaches a constant maximum at about $t = 2500$. The chain of $L = 125$, however, exhibits periods of metastability followed by large fluctuations in the local order

parameter. Moreover, the maximum of its order parameter never equals or exceeds the maximum of the $L = 100$ case.

In secondary nucleation, one major difference in the assumptions of the current models is whether the simultaneous adsorption of many chains on the growth front has a disruptive effect on the growth rate or the perfection of the crystal. In an effort to address this issue, we have considered the simultaneous crystallization of 20 chains of length 140 onto a template. As an example, the template is prepared in the following manner. First, 8 chains of length 250 are allowed to crystallize together. In the resulting crystal, each chain has folded into 4 stems whose length is about 60 united atoms. The crystal is then pressed flat using hard boundary conditions into a two layer thick crystal. This flat crystal is then fixed in space and placed near one surface within a cubic box 100 bond lengths on each side. Into this box we randomly place 20 disordered chains of length 140 and commence the simulation at $T^* = 10$. The results are shown in Figure 4.7.

From the initial state, chains which are close to the growth front are pulled in and rapidly crystallized, adding one layer to it. Chains which are far from the attractive influence of the growth front undergo homogeneous nucleation. Through random forces, the free nucleus eventually drifts near enough to the growth front to interact with it. The chain ends act as 'feelers' which align the free nucleus with the growth front. Interestingly, the free nucleus merges with the growth front by sliding itself in from the side. It is not known how common this kind of event is. Close observations of individual chains on the growth front reveals substantial stem mobility on the surface but insignificant activity inside. Figure 4.7(f) is an end-view showing the arrangement of stems on the crystal. At lower temperatures there would be insufficient mobility even at the surface, arresting the growth process. It was also observed that during the merging of the two nuclei, the motion of individual

chains of the free nucleus is akin to that of a worm, with surges of forward motion extending the chain followed by relaxation periods in which the tail pulls up. This worm-like collective behavior is unexpected and merits further study.

4.5 Multi-chain primary nucleation

Unless polymers are in extremely dilute solutions, it is unlikely that nucleation occurs as single-chain events. In multi-chain primary nucleation, entanglements are expected to play a major role kinetically. Given that there are entanglements present in aggregates and that entanglements are a kinetically-influencing factor, we address the question of how multi-chain nucleation differs from short, single-chain nucleation.

A series of simulations have been performed to measure the effect of chain length on the crystallization behavior. Because crystal size affects the kinetics of crystallization, it is kept constant, constrained to contain approximately 2000 beads. As the chain length varies, the number of chains varies to satisfy the constraint. The melting point for systems of this size has been estimated to be approximately $T^* = 11.5$. The crystallizations described here are performed isothermally at $T^* = 11$ so that the higher mobilities would enable the kinetics to proceed at a faster rate.

Similar to the single-chain nucleation, multi-chain nucleation is characterized by the simultaneous development of local order everywhere followed by a global restructuring. This is apparent in Figure 4.8. Interestingly, after the aggregate has become a single crystal, lamellar thickening is observed, both visually in frames (d) through (f) in Figure 4.8 as well as in the plot of the radius of gyration of the crystal in Figure 4.9.

The formation of a crystal follows kinetically favorable paths. The first nuclei formed from the disordered state have many more conformations trapped in the gauche state than that in the thermodynamic equilibrium at a given T^* below T_m^* (11.5). Thus, the initial nuclei tend to be small and thin. However, once a lamella has formed, it is akin to being in a glassy state where the degrees of freedom are limited. The exact mechanism of the lamellar thickening process is unclear, but graphic visualizations of the process reveal collective motion among chains. The driving force for this collective motion is the gain in energy that arises from the enhancement of the number of nearest-neighbor contacts accompanied by a reduction of the number of folds per chain. The visual displays at finer time intervals reveal that the stems act collectively and that there is a continuous motion of folds. Soon, there is a population of chains with less folds and therefore lower energy. The process continues until the number of folds per chain within the lamella has decreased by one. This process may repeat as the lamella thickens.

This process occurs surprisingly fast and it is separated by periods of quiescence. In Figure 4.9 the radius of gyration of the crystal can be seen to jump from a 4-fold to a 3-fold to a 2-fold lamella. At this point it is not clear whether during the periods of quiescence the lamella is undergoing internal reorganization or whether it simply represents an activation barrier to thickening. The simulation was carried out to 50,000 time units with no further thickening observed.

These observations are in qualitative agreement with recent experimental results of Alamo *et al.* [89] on toluene solutions of *n*-alkanes crystallized at various temperatures. For this system the authors have observed that the *n*-alkanes first adopt the once-folded configuration then recrystallize into the extended-chain configuration. At higher temperatures, these two events move closer in time until only one broad exotherm is detected in the DSC. The interesting part of the result is

that at the lower temperatures, the recrystallization peak is quite distinct. This shows that the transition from folded to extended chains occurs abruptly and furthermore, since the polyethylene solution undoubtedly contained many lamellae, the majority of them had the same time delay between initial crystallization and lamellar thickening.

If the simulation is run for a reasonably long time after thickening one may assume that it is close to having the equilibrium number of folds per chain. As the chain length increases, the number of folds per chain will also increase. As we have shown before, the chain length will always be an integer multiple of lamellar thickness at least for the range of chain lengths that are simulated (up to 400 united atoms). The ratio of chain length to the lamellar length is plotted in Figure 4.10 against the chain length. In this figure we have also included the classic results of Ungar *et. al.* [79] on *n*-alkanes measured by low-frequency Raman spectroscopy in the longitudinal acoustic mode. Multiple data points at the same chain length represent samples crystallized under different conditions.

4.6 Conclusions

Using Langevin dynamics, we have simulated polymer crystallization in the regimes of single- and multi-chain homogeneous nucleation and of secondary nucleation and growth. We have shown that polymer crystallization is characterized by the competition between configurational entropy in the available torsional states and the enthalpy of the Lennard-Jones attraction. It is also strongly affected by the slow kinetics associated with chain entanglements.

Our results show that for relatively short single-chain crystallization where entanglement is not an important factor, the local orientational order parameter dis-

plays a sharp initial increase followed by a plateau, while the global orientational order parameter increases more gradually. The time sequence figures confirm the model in which straight segments form rapidly and assemble in small domains while over longer times the chain readjusts itself into a more perfect crystal. Qualitative agreement with theory and experiments is found for the lamellar thickness of a single folded chain at various degrees of undercooling.

The first attempt at understanding crystal growth has been made by creating a fixed surface as a model for the growth front and placing single chains of various lengths near it to observe adsorption and secondary nucleation. It has been found that chains whose lengths are integer multiples of the growth front thickness crystallize readily while other chains are only in metastable, semicrystallized states. When many chains are near a growth front, it has been shown that the crystal growth is very complex. At lower temperatures and lower mobilities we expect the orderly growth process to break down.

We report progress in the understanding of lamellar thickening. Though the dimensions of the lamellae that are simulated are small (the thickness being greater than the width) the simulations nevertheless illustrate the kind of necessary cooperative motion among chains if lamellar thickening is to occur. The thickening process occurs in discrete steps and the fold lengths display quantization as observed experimentally[88, 89]. The lamellar thicknesses versus chain length also corresponds well with experimental studies on long monodisperse *n*-alkanes [79].

The Langevin dynamics model described in this chapter has been shown to produce experimentally observed results in a reliable manner. It has provided insight into previously-unknown details of the crystallization process. It is our goal that this model be leveraged in future studies in other crystallization regimes and new molecular architectures.

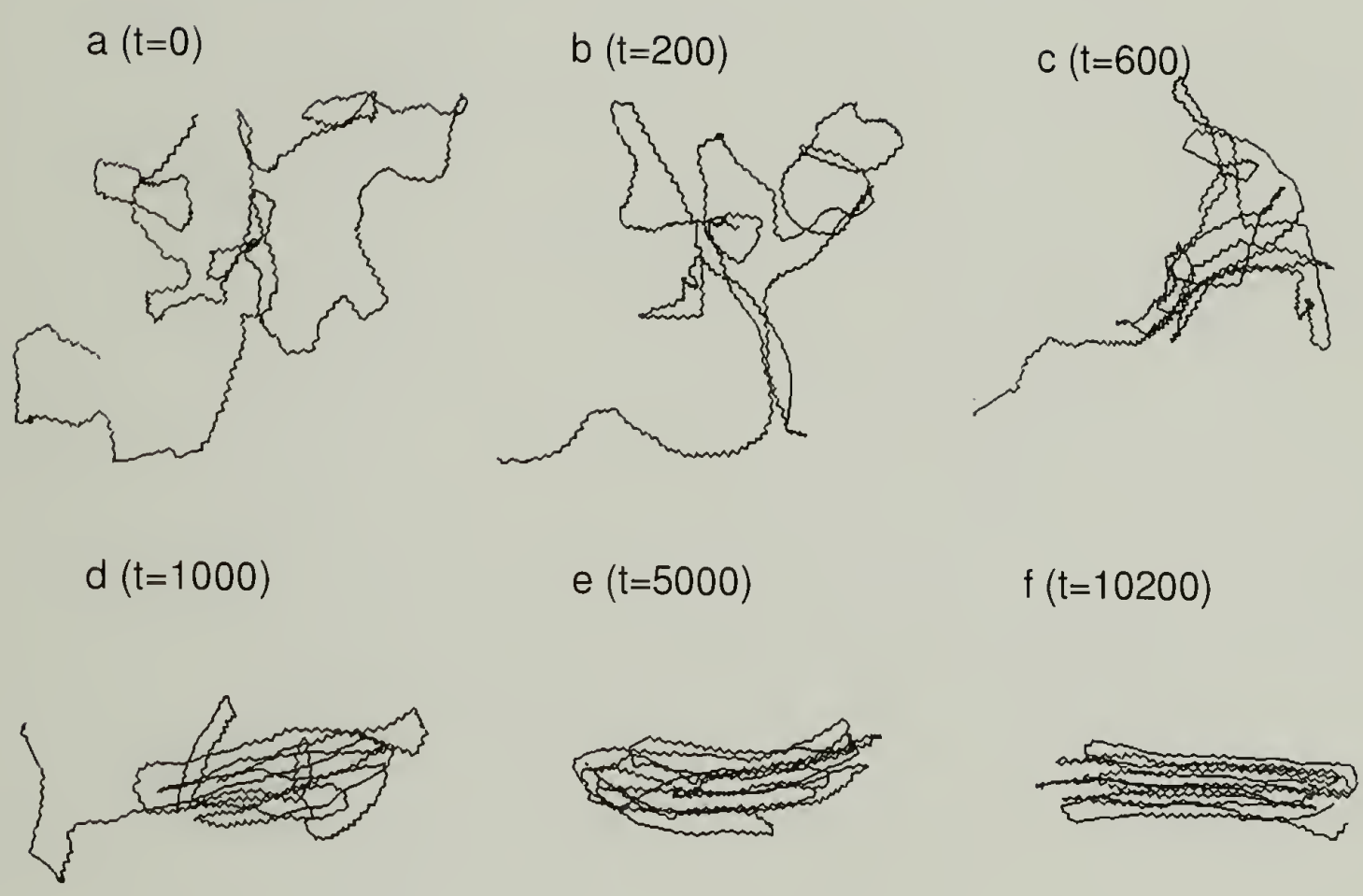

Figure 4.1 Primary nucleation sequence of L=700 chain quenched from $T^* = 12$ to $T^* = 9$. Local chain alignment is initiated at various sites in the early stages followed by global alignment at later times.

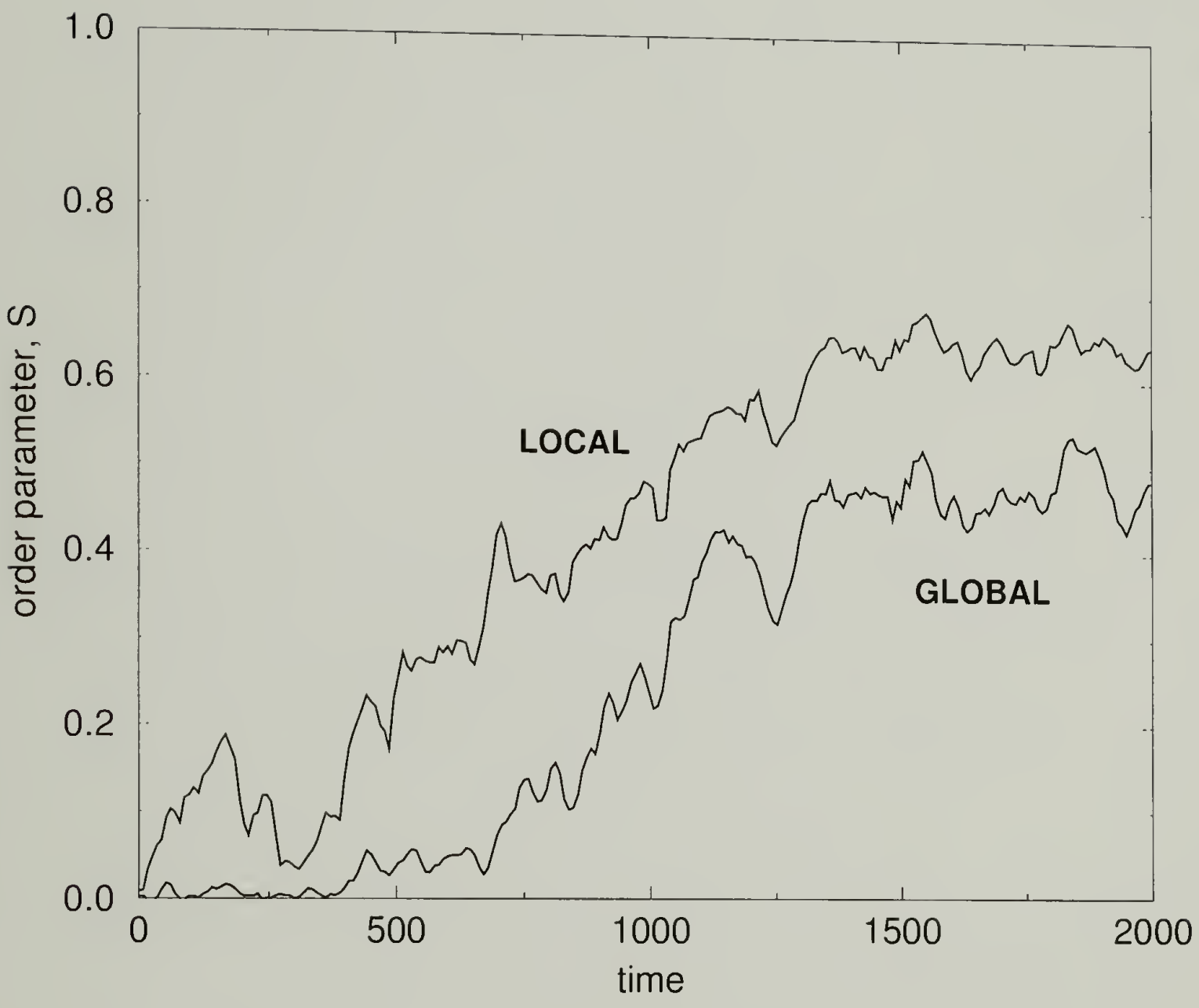

Figure 4.2 Order parameter development of sequence shown in Figure 4.1. Local ordering appears before global ordering.

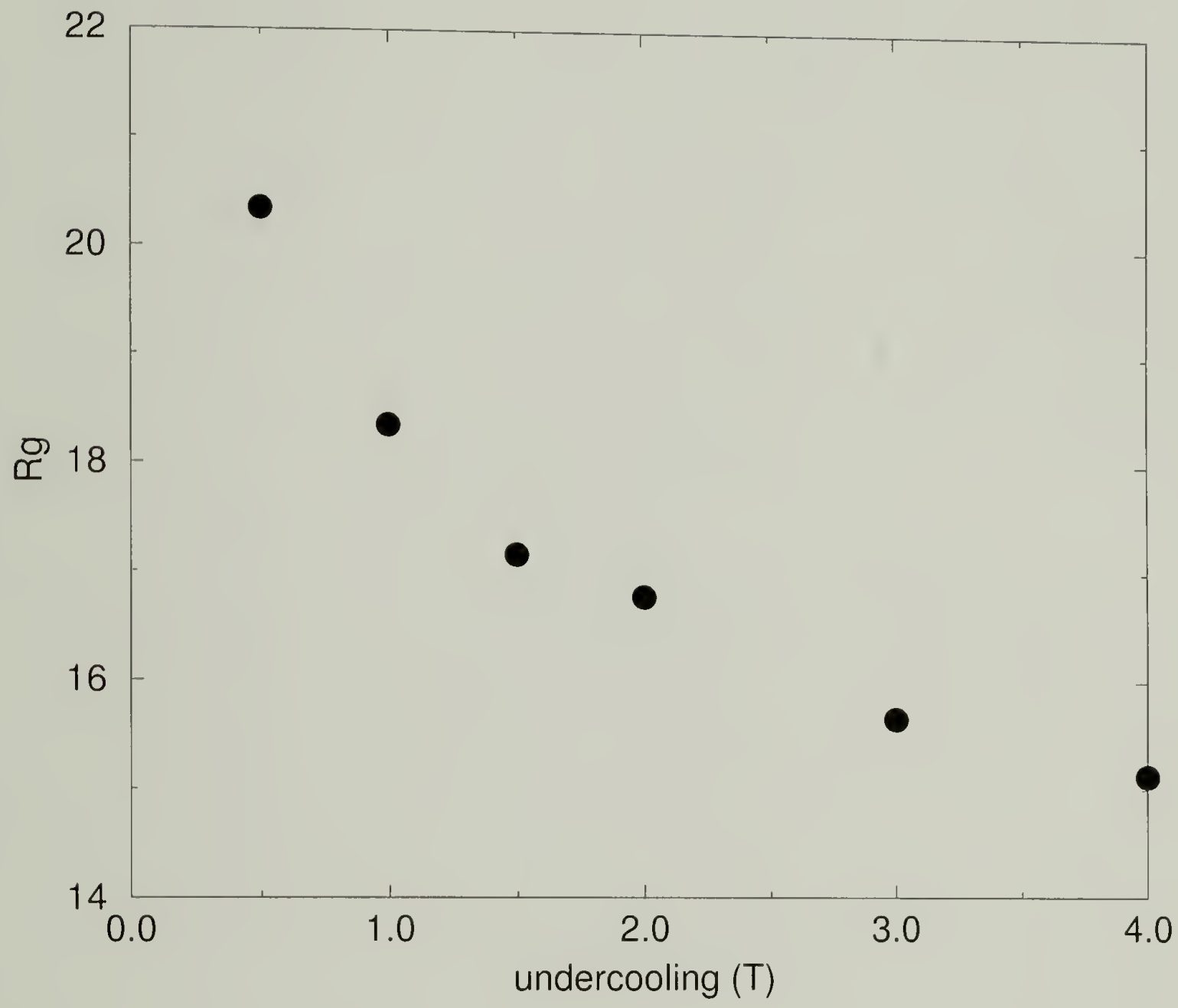

Figure 4.3 Lamellar thickness (expressed as R_g) versus undercooling for chains of L=500. Each data point is the average of four chains. Curve follows the $1/\Delta T^*$ relationship.

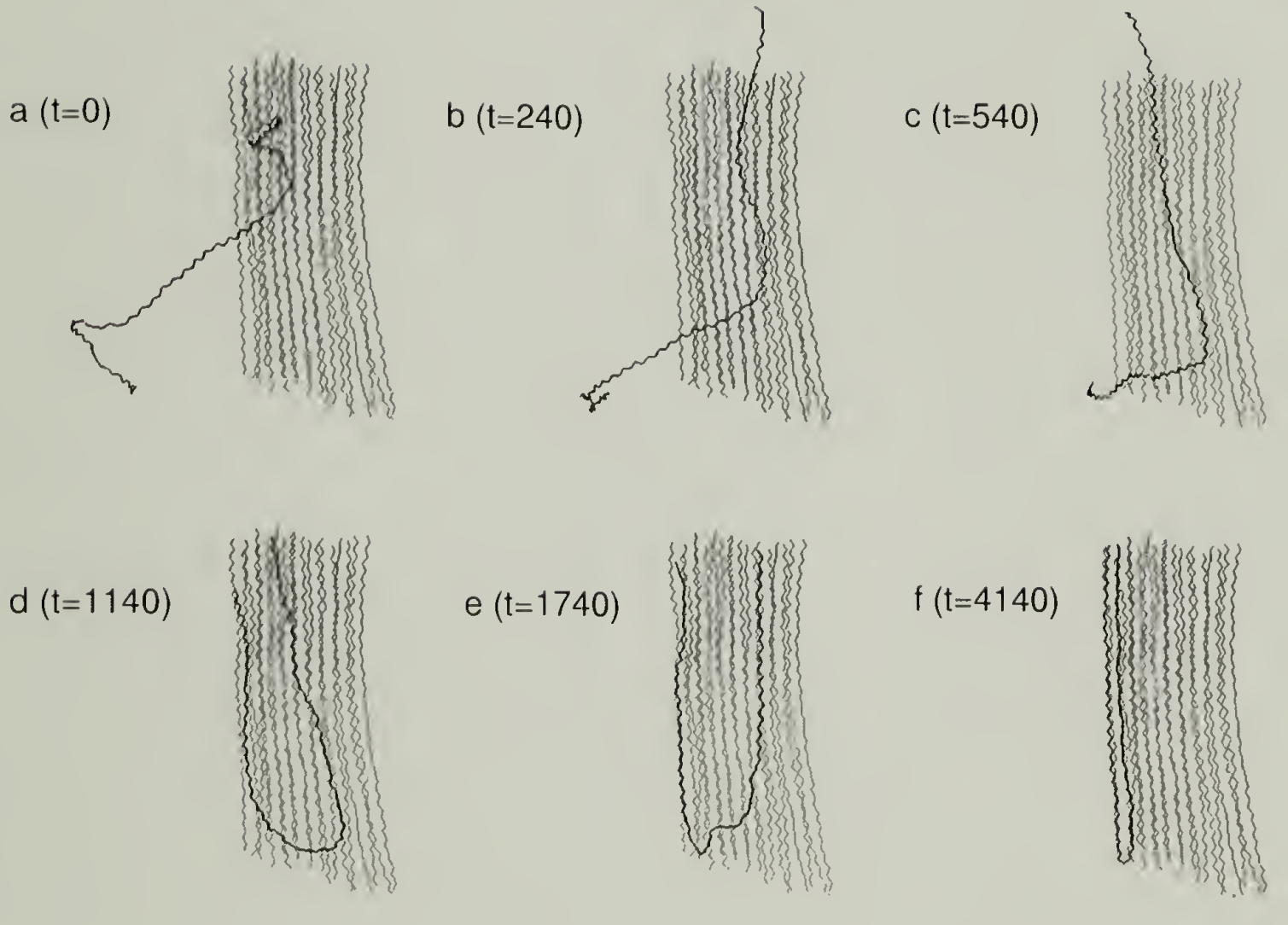

Figure 4.4 Attachment of L=100 chain onto L=50 growth front model. Growth front chains are immobilized. The chain exhibits significant mobility (a)-(e) before it establishes perfect registration with the surface (f).

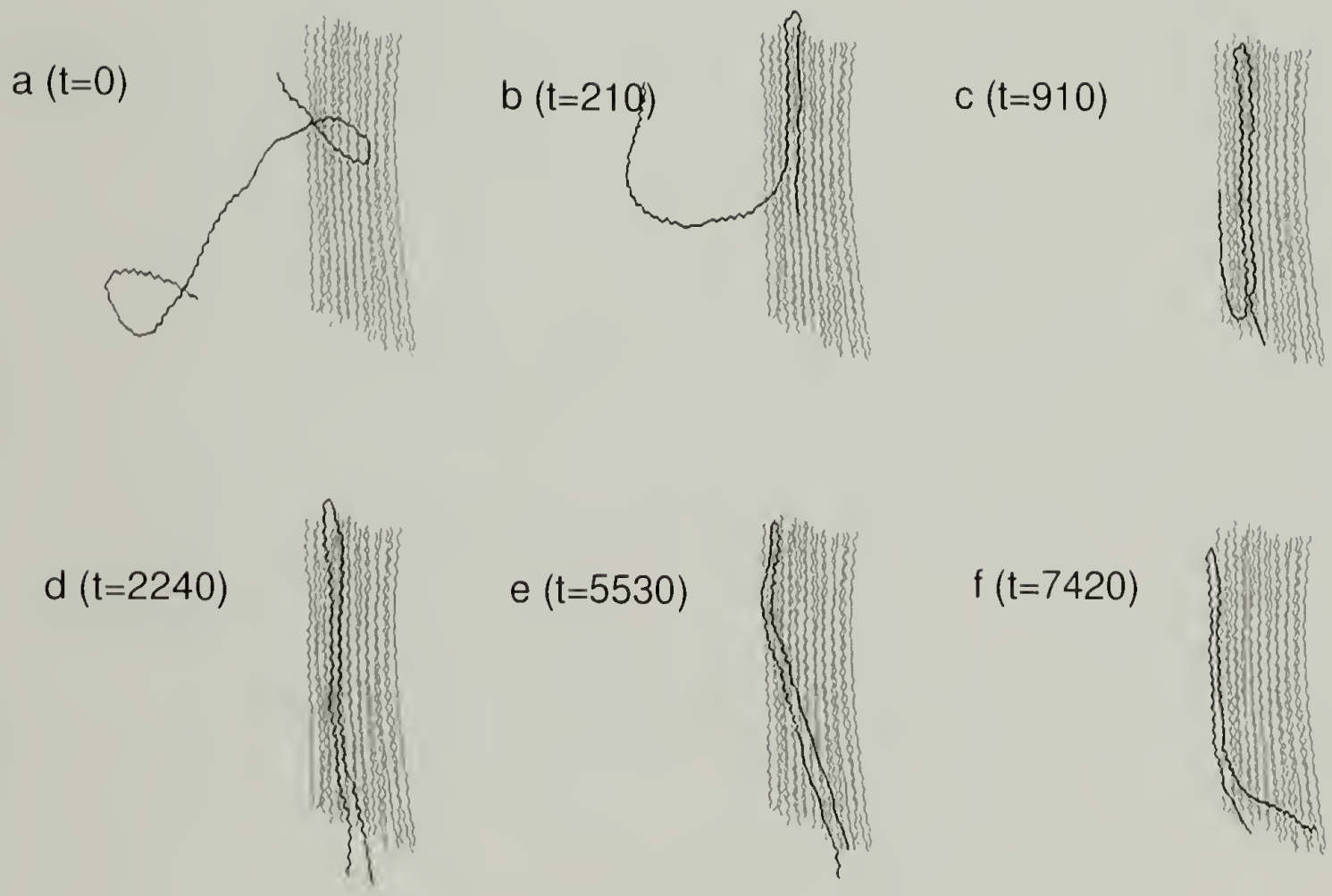

Figure 4.5 Attachment of a L=125 chain onto L=50 growth front model. Growth front chains are immobilized. The chain adopts only metastable configurations.

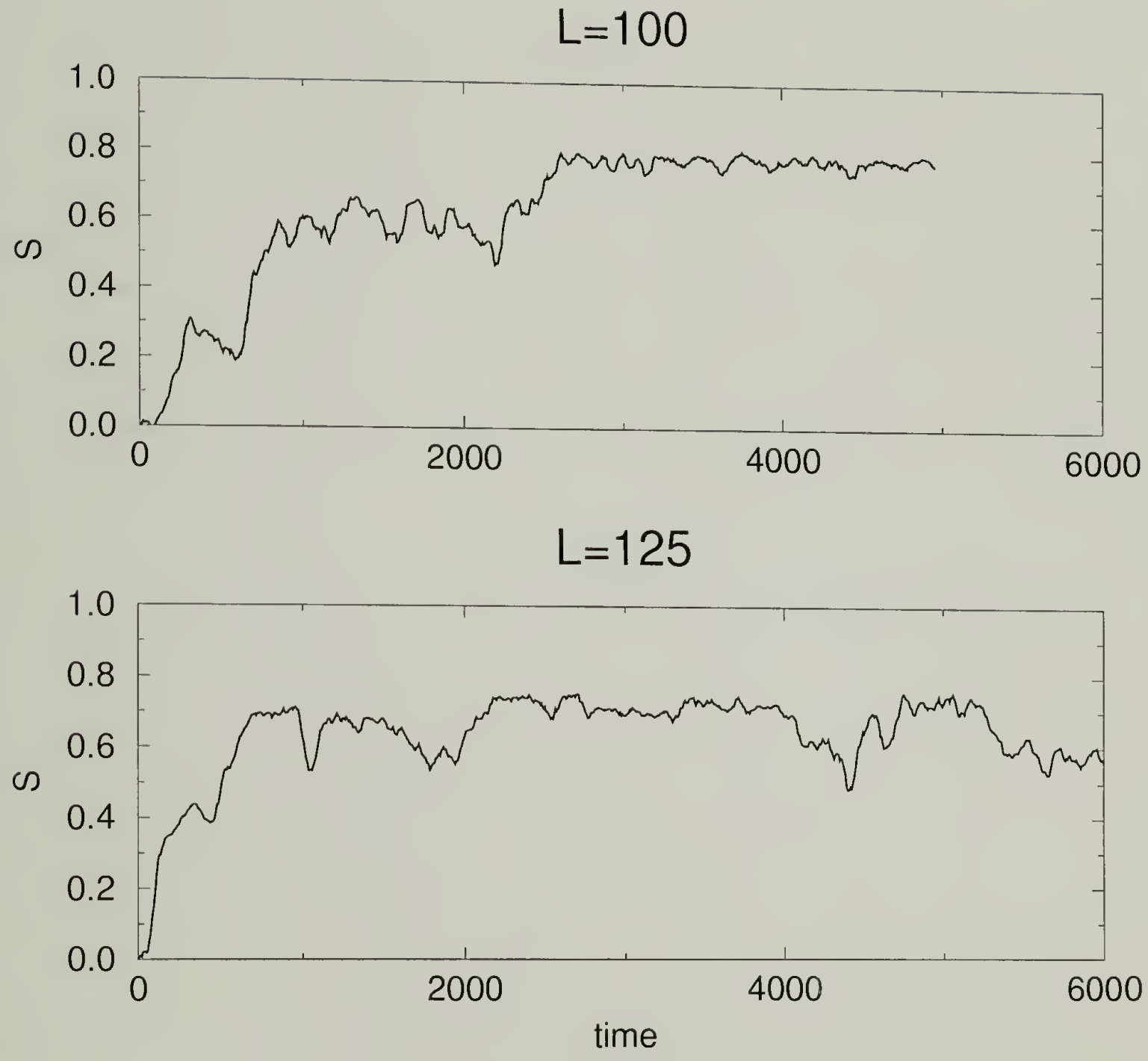

Figure 4.6 Comparison of order parameter for L=100 and L=125 chains from Figures 4.4 and 4.5. The stability differences between chains of integer multiple lengths versus mismatched chains is evident.

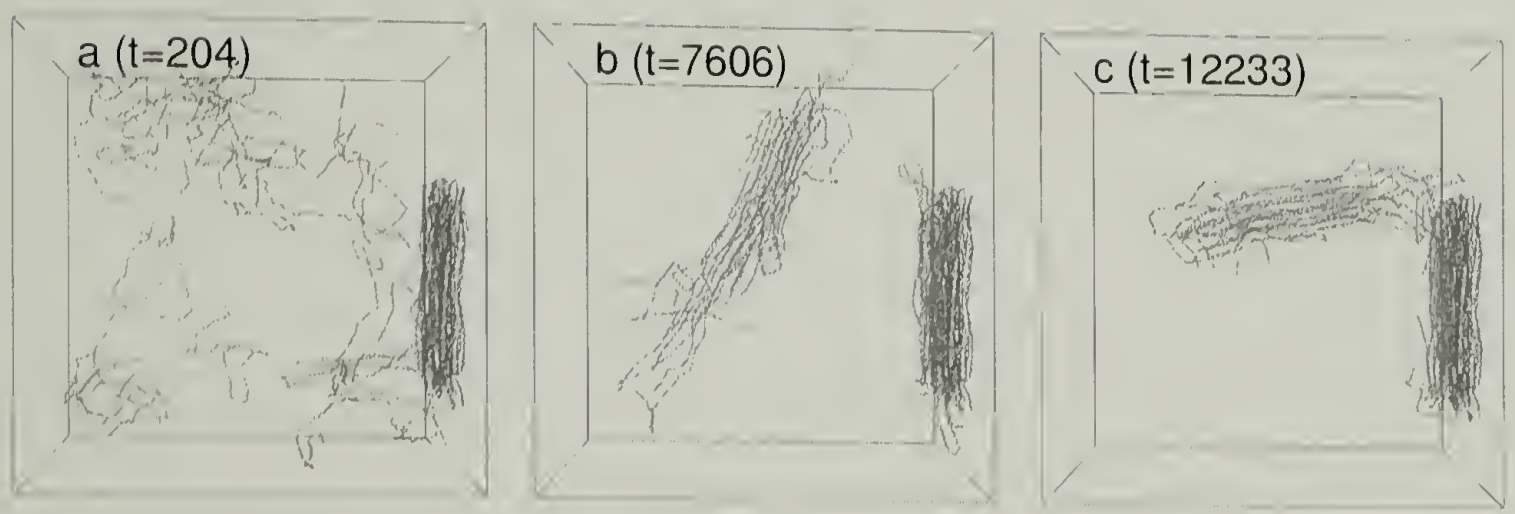

Figure 4.7 Simulation of 8 chains of L=250 near a fixed crystalline surface. (a)-(e) show simultaneous homogeneous and heterogeneous nucleation and subsequent interaction of the two nuclei. (f) is the end-view of (e) showing arrangement of stems on the surface.

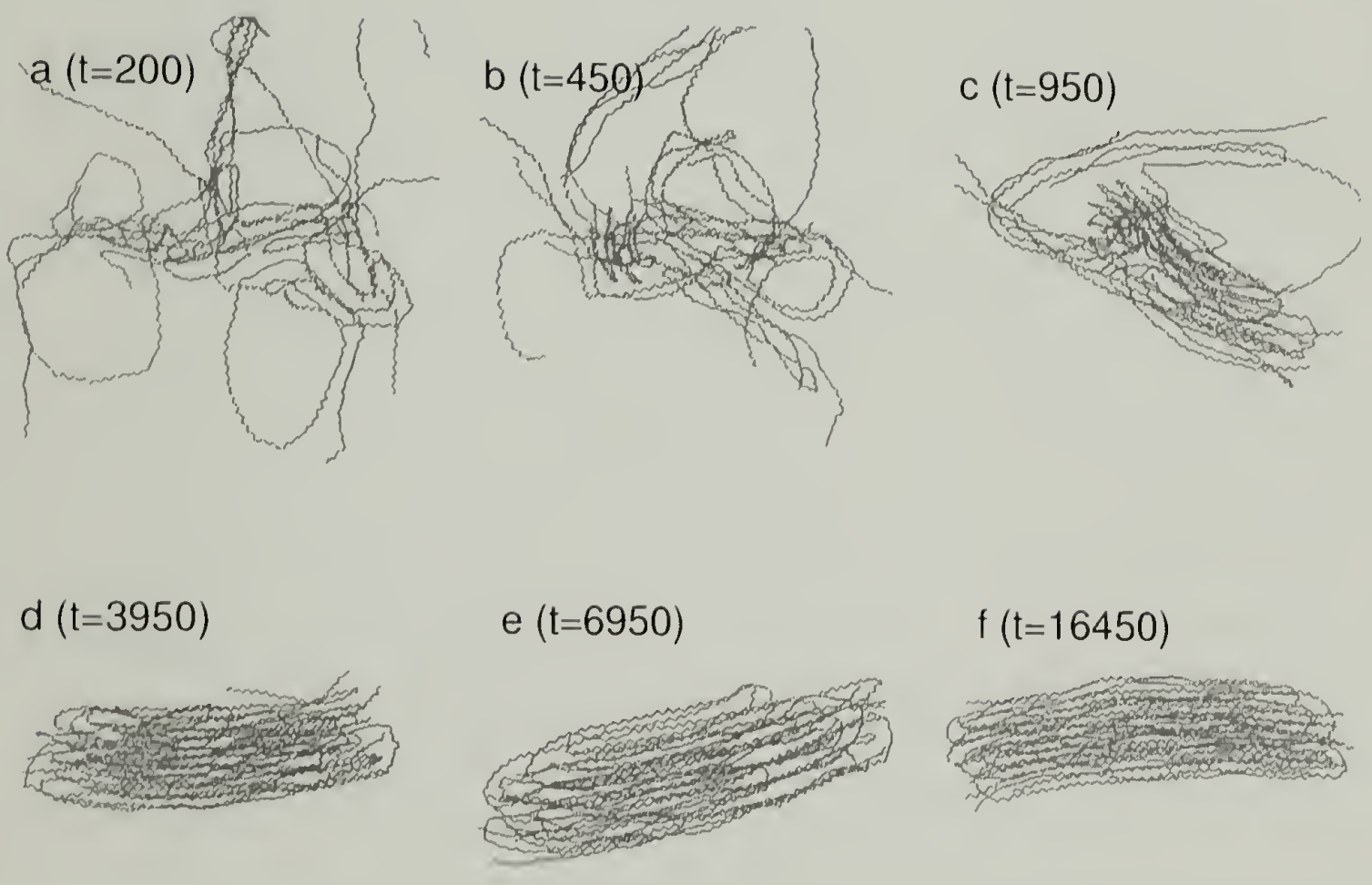

Figure 4.8 Multi-chain primary nucleation. 13 chains of L=154 are quenched simultaneously. Lamellar thickening is apparent in frames (d)-(f).

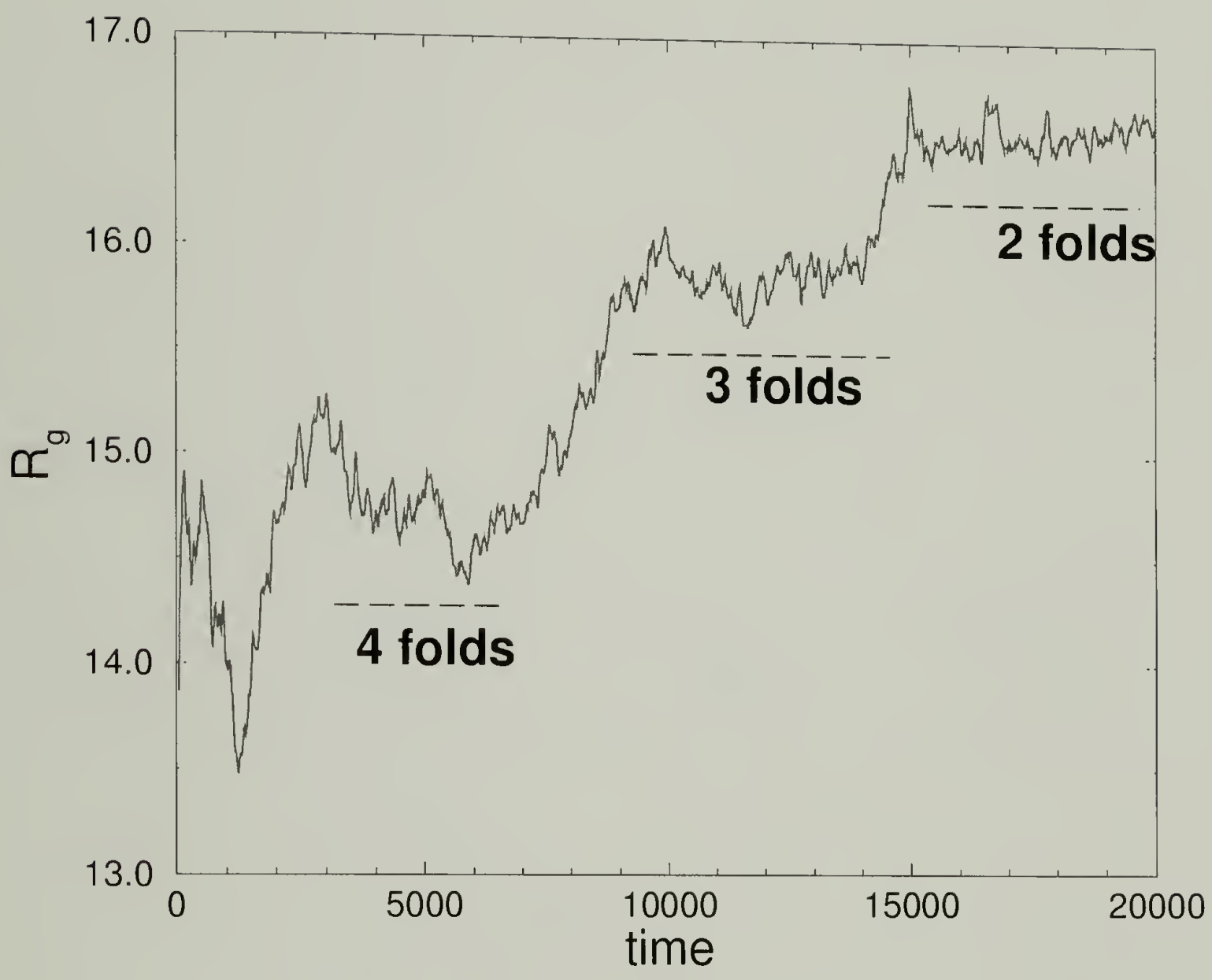

Figure 4.9 Radius of gyration for multi-chain crystallization sequence in Figure 4.8. Lamellar thickening occurs in rapid steps separated by periods of relative quiescence.

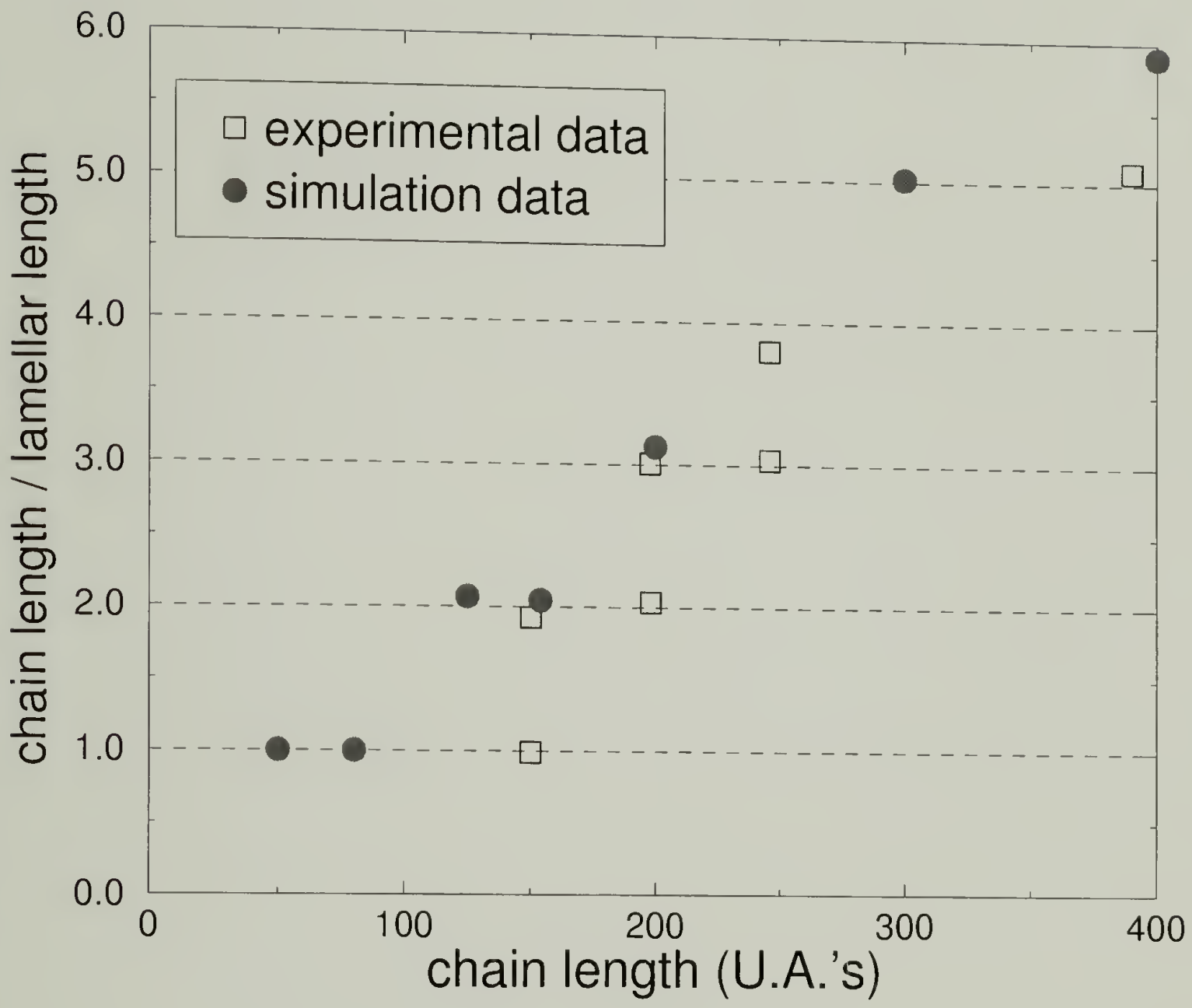

Figure 4.10 Chain lengths are observed to be integer multiples of lamellae thicknesses. This shows that lamellae are made of complete rather than partial stems. Simulation results agree with experimental results by Ungar and co-workers.

CHAPTER 5

CONCLUSIONS AND FUTURE WORK

5.1 Liquid Crystal Defect Annihilation

In the ongoing debate in the liquid crystal community over whether defect annihilation kinetics follow mean-field or other theories, we provide support for the view that the scaling with time is not as high as the mean-field prediction of -1. We have generalized an existing theory to support the value of -6/7 in both two and three dimensions. The physical reason for the non-mean-field result may be the fact that the background potential experienced by each defect is not constant but instead is changing as defects repel or attract. Frustrated arrangements of defects slow the kinetics of the system accordingly. In addition, we have investigated the effect of various parameters of the extended Frank free energy equation, which include elastic constants, temperature, field strength, and surface interaction energy. We found that varying the elastic constants has no effect on the scaling, temperature likewise has no effect until the nematic-isotropic transition point is approached, applying an external field above the Freedericks transition changes the system kinetics from a power law to an exponential decay, and varying the surface interaction energy has systematic effects on defects near the surface.

In three dimensions, there is unfinished work in the study of defect lines. We have found that defect lines are not of the same sign along their contour. If the

signs of the defects are analogous to electrical charges, then these defect lines are analogous to polyampholytes and not polyelectrolytes. Defect lines however are massless and once annihilated, do not regenerate the same sequence. We wish to know how the "charge sequence" of a defect line evolves over time.

We have barely scratched the surface of the rich subject of liquid crystals in this research. From an engineering point of view, they are now quite well understood, with many technical hurdles having been already overcome. For example, adding small amount of cholesteric (having chirality and twist) liquid crystals of the same chirality to nematic liquid crystals will impart a predictable twist to liquid crystals placed between perpendicularly-oriented brushed plates. This eliminates the constant appearance and disappearance of defects as externally-applied electric fields switch the orientation. Of greatest importance to engineers is the minimization of response time to external fields. Modern displays require the pixels in LCD's to switch at least 60 times per second over a macroscopic distance. Failure to do so results in ghosting. In future work, we wish to revisit the original subject of polymer-dispersed liquid crystals. Since PDLC's rarely contain perfectly spherical droplets, the effect of droplet asymmetry is important. In fact, the ellipticity of droplets can be exploited, forcing the orientation to return more quickly to a given orientation once the external field has been turned off.

5.2 Liquid Crystal Inversion Walls

The subject of liquid crystal inversion walls is relatively esoteric and can be observed only under specially designed conditions. They are, however, related to the much larger subject of walls studied in the field of magnetism. We have undertaken to verify a simple theoretical prediction by de Gennes and Brochard

which calls for the radius of inversion loops to scale with time as $t^{-1/2}$. Similar to the other section on liquid crystal annihilation kinetics, we have examined the kinetics as a function of the various parameters such as temperature, field strength, and elastic anisotropy, and found them to satisfactorily agree with the expected results. Because the loops are simulated in isolation, possible interactions that might exist in a random distribution of loops are not considered.

Visual representation of the simulation results in two dimensions are consistent with those from cross-polar microscopy of thin films. To date, however, we do not know of experimental observations of three-dimensional walls predicted by our simulations. This can be attributed to the lack in general interest in this subject as well as the difficulty of imaging three dimensional objects having very little contrast. One possible technique would be microtoming of frozen polymer liquid crystals and reassembling of the three-dimensional structure.

5.3 Polymer Crystallization

Polymer crystallization is a very broad subject with many avenues of exploration available. Not only are there distinct stages during crystallization each of which can be scrutinized, there are endless variations possible in monomer properties, chain architectures, monomer sequences, etc. We have chosen to study the very basic and generic model of simple, homogeneous, linear chains. From these studies we have been able to point out the general features common to crystallization processes. One of these is the importance of fluctuation in both density and orientation that serve as potential nucleation sites. The other is the need for the persistence length to be long enough to favor a high percentage of linear segments.

Many conclusions and new insights were drawn from this study. The reader is

referred to the conclusion section of chapter 4 for details. The most striking new insight to us is the degree of cooperativity that occurs during lamellar thickening. Intuitively, one might expect thickening to be a sporadic process dictated by the random pull-out or pull-through of chain stems and chain ends. Instead, we observe that thickening occurred abruptly with nearly all chains undergoing simultaneous change in conformation. This rather exciting result warrants further study. As of yet it is unclear whether the folded chains extend via a mechanism where all stems lengthen simultaneously or whether one stem might initially unfold followed by other stems lengthening to re-absorb the dangling end into the crystal.

For other future work we would like to extend the current progress made on the study of branched chains. Preliminary simulations have demonstrated how in some cases branching severely diminishes the degree of crystallization but in other cases actually enhances crystallization by establishing well-defined folding points.

The ability to simulate melt crystallization remains one of the holy grails of simulation. The sheer number of interacting monomers required to perform an adequate simulation has left this problem open for future generations of researchers. With so many applications dependent on processed semicrytalline polymers in the bulk, the ability to predict and control crystallization behavior will have great value to scientists and industry alike.

BIBLIOGRAPHY

[1] C. Robinson, Trans. Faraday. Soc., **52**, 571 (1956).

[2] J.R. Hobdell and A.H. Windle, J. Chem. Soc. Faraday Trans. **91**, 2497 (1995).

[3] M.J.E. O'Rourke and E.L. Thomas, MRS Bulletin, Sept, 29 (1995).

[4] M. Kleman, MRS Bulletin, Sept, 23 (1995).

[5] A. Ciferri, *Liquid Crystallinity in Polymers*, (VCH, New York, 1991).

[6] D.-K. Ding and E. L. Thomas, Macromolecules **26**, 6531 (1993).

[7] O. D. Lavrentovich and S. S. Rozhkov, JETP Lett. **47**, 254 (1988).

[8] T. H. O'Dell, *Ferromagnetodynamics*, John Wiley & Sons, New York (1981).

[9] L. Leger, Mol. Cryst. Liq. Cryst. **24**, 33 (1973).

[10] K. Binder, *Applications of the Monte Carlo Method in Statistical Physics*, (Springer-Verlag, New York, 1984).

[11] D. C. Rapaport, *The Art of Molecular Dynamics Simulation*, (Cambridge, Cambridge, 1995).

[12] M. P. Allen and D. J. Tildesley, *Computer Simulation of Liquids* (Clarendon, Oxford, 1987).

[13] F. von Goeler, M. Muthukumar, Macromolecules, **28**, 6608 (1995).

[14] P. Welch, private communication.

[15] Y. Akpalu, private communication.

[16] G.P. Crawford and J.W. Doane, Cond. Mat. News, **1**, 5 (1992).

[17] S. Chandrasekhar, *Liquid Crystals*, Cambridge University Press, Cambridge (1992).

[18] P.G. deGennes and J. Prost, *The Physics of Liquid Crystals*, Oxford University Press, New York (1993).

[19] M. Kleman, *Points, Lines and Walls: In Liquid Crystals, Magnetic Systems, and Various Ordered Media*, John Wiley , New York (1983).

[20] M. Mermin, Rev. Mod. Phys. **51** 591 (1979).

[21] M. Salomaa and G. Volovik, Rev. Mod. Phys. **59**, 533 (1987).

[22] A. Vilenkin and E.P.S. Shellard, *Topological Defects and Cosmology*, Cambridge University Press, Cambridge (1994).

[23] C. Y. Young, R. Pindak, N.A. Clark, and R.B. Meyer, Phys. Rev. Lett. **40**, 773 (1978).

[24] R. Pindak, C.Y. Young, R.B. Meyer, and N.A. Clark, Phys. Rev. Lett. **45**, 1193 (1980).

[25] H. Orihara and Y. Ishibashi, J. Phys. Soc. Jpn. **55**, 2151 (1986).

[26] T. Nagaya, H. Orihara and Y. Ishibashi, J. Phys. Soc. Jpn. **56**, 1898 (1987); **59**, 377 (1990).

[27] T. Shiwaku, A. Nakai, H. Hasegawa, and T. Hashimoto, Polymer Commun. **28**, 174 (1987).

[28] S. Rojstaczer and R.S. Stein, Mol. Cryst. Liq. Cryst. **157**, 293 (1988).

[29] T. Hashimoto, A. Nakai, H. Hasegawa, S. Rojstaczer and R.S. Stein, Macromolecules **22**, 422 (1989); **23**, 1590 (1993).

[30] T. Shiwaku, A. Nakai, H. Hasegawa and T. Hashimoto, Macromolecules **23**, 1590 (1990).

[31] I. Chuang, R. Durrer, N. Turok and B. Yurke, Science **251**, 1336 (1991).

[32] T. Nagaya, H. Hotta, H. Orihara and Y. Ishibashi, J. Phys. Soc. Jpn. **60**, 1572 (1991); **61**, 3511 (1992).

[33] B. Yurke, A.N. Pargellis and N. Turok, Mol. Cryst. Liq. Cryst. **222**, 195 (1992).

[34] B. Yurke, A.N. Pargellis, I. Chuang and N. Turok, Physica B**178**, 56 (1992).

[35] A.N. Pargellis, P. Finn, J.W. Goodby, B. Yurke and P.E. Cladis, Phys. Rev. A**46**, 7765 (1992).

[36] N. Mason, A.N. Pargellis and B. Yurke, Phys. Rev. Lett. **70**, 190 (1993).

[37] D-K. Ding and E.L. Thomas, Mol. Cryst. Liq. Cryst. **241**, 103 (1994).

[38] T. Nagaya, H. Orihara and Y. Ishibashi, J. Phys. Soc. Jpn. **64**, 78 (1995).

[39] D. Toussaint and F. Wilczek, J. Chem. Phys. **78**, 2642 (1983).

[40] H. Toyoki, Phys. Rev. A**42**, 911 (1990).

[41] H. Toyoki, Phys. Rev. B**45**, 1965 (1992).

[42] A.J. Bray and S. Puri, Phys. Rev. Lett. **67**, 2670 (1991).

[43] A.J. Bray and K. Humayun, J. Phys. A**25**, 2191 (1992).

[44] R.E. Blundell and A.J. Bray, Phys. Rev. A**46**, R6151 (1992).

[45] A.J. Bray, Phys. Rev. E**47**, 228 (1993).

[46] A.J. Bray, Physica A**194** 41 (1993).

[47] M. Mondello and N. Goldenfeld, Phys. Rev. A**42**, 5865 (1990); A**45**, 657 (1992); E**47**, 2384 (1993).

[48] F. Liu and G.F. Mazenko, Phys. Rev. B**46**, 5963 (1992); **47**, 2366 (1993).

[49] H. Orihara and Y. Ishibashi, J. Phys. Soc. Jpn. **61**, 1 (1992).

[50] B. Yurke, A.N. Pargellis, T. Kovacs and D.A. Huse, Phys. Rev. E**47**, 1525 (1993).

[51] H. Toyoki, J. Phys. Soc. Jpn. **63**, 4446 (1994).

[52] S.E. Bedford and A.H. Windle, Liq. Cryst. **15**, 31 (1993).

[53] A.H. Windle, H.E. Assender and M.S. Levine, Proc. R. Soc. London A**348**, 73 (1994).

[54] W.G. Jang, V.V. Ginzburg, C.D. Munzy and N.A. Clark, Phys. Rev. E**51**, 411 (1995).

[55] W. Helfrich, Phys. Rev. Lett. **28**, 1518 (1968).

[56] F. Bloch, Zeit. für Phys. **74**, 295 (1932).

[57] L. Neel, Rend. Acad. Sci. Paris **241**, 533 (1955).

[58] P. G. deGennes, *Molecular Fluids*, Gordon and Breach, London (1973).

[59] F. Brochard, J. de Phys. **33**, 607 (1972).

[60] P. G. deGennes, Mol. Cryst. Liq. Cryst. **12**, 193 (1971).

[61] C. Gähwiller, Mol. Cryst. Liq. Cryst. **20**, 301 (1973).

[62] F. C. Frank, Disc. Faraday Soc. **25**, 19 (1958).

[63] A. Sharples, *Introduction to Polymer Crystallization* (Edward Arnold Ltd., London, 1966).

[64] L. Mandelkern, *Crystallization of Polymers* (McGraw-Hill Inc., New York, 1964).

[65] J. D. Hoffman and R. L. Miller, Polymer **38**, 3151 (1997).

[66] K. Armistead and G. Goldbeck-Wood, Adv. in Polym. Sci. **100**, 219 (1992).

[67] E. A. DiMarzio, C. M. Guttman, and J. D. Hoffman, Faraday Discuss. Chem. Soc. **68**, 210 (1979).

[68] J. D. Hoffman, C. M. Guttman, and E. A. DiMarzio, Faraday Discuss. Chem. Soc. **68**, 177 (1979).

[69] P. J. Flory and D. Y. Yoon, Faraday Discuss. Chem. Soc. **68**, 389 (1979).

[70] A. Keller, Phil. Mag. **2**, 1171 (1957).

[71] J. D. Hoffman, G. T. Davies, J. I. Lauritzen, Treatise on solid-state chemistry, vol. 3 (Plenum, New York, 1976).

[72] D. M. Sadler, Polymer **24**, 1401 (1983).

[73] D. M. Sadler and G. H. Gilmer, Phys. Rev. Lett. **56**, 2708 (1986).

[74] D. M. Sadler, Nature **326**, 174 (1987).

[75] F. C. Frank and M. Tosi, Proc. Royal Soc. A **263**, 323 (1961).

[76] J. J. Point, Macromolecules **12**, 770 (1979).

[77] T. A. Kavassalis and P. R. Sundararajan, Macromolecules, **26**, 4144 (1993).

[78] P. R. Sundararajan and T. A. Kavassalis, J. Chem. Soc. Faraday **91**, 2541 (1995).

[79] G. Ungar, J. Stejny, A. Keller, I. Bidd, and M. C. Whiting, Science **229**, 386 (1985).

[80] T. Yamamoto, J. Chem. Phys., **107**, 2653 (1997).

[81] W. Paul, D. Y. Yoon, and G. D. Smith, J. Chem. Phys. **103**, 1702 (1995).

[82] S. Toxvaerd, J. Chem. Phys. **93**, 4290 (1990).

[83] B. G. Sumpter, D. W. Noid, G. L. Liang, and B. Wunderlich, Adv. in Polym. Sci. **116**, 73 (1994).

[84] W. C. Swope, H. C. Andersen, P. H. Berens, and K. R. Wilson, J. Chem. Phys. **76**, 637 (1982).

[85] C. W. Gear, Report ANL 7126, (Argonne National Laboratory, 1966).

[86] S. J. Organ and A. Keller, J. Mater. Sci. **20**, 1602 (1985).

[87] P. G. Higgs and G. Ungar, J. Chem. Phys. **100**, 640 (1994).

[88] W. M. Leung, R. St. J. Manley, and A. R. Panaras, Macromolecules **18**, 746 (1985).

[89] R. G. Alamo, L. Mandelkern, G. M. Stack, C. Krohnke, and G. Wegner, Macromolecules **27**, 147 (1994).